Journal of Materials Processing Tech. 343 (2025) 118998

Contents lists available at ScienceDirect

Journal of Materials Processing Tech.

journal homepage: www.elsevier.com/locate/jmatprotec

Research article

Engineering heterostructures via layer-wise in-situ alloying in additive manufacturing: Compositional and architectural design in heterogeneous 316 L stainless steel for strength-ductility synergy

Yicheng Wang [a,1], Qihang Hu [a,1], Zhihong Yao [a], Bo Mao [b], Gangxian Zhu [a,*], Jiaqiang Li [a,*], Xing Zhang [a,*,2]

[a] School of Mechanical and Electrical Engineering, Soochow University, Suzhou, Jiangsu 215000, China
[b] School of Materials Science and Engineering, Shanghai Jiao Tong University, Shanghai 200240, China

ARTICLE INFO

Keywords:
Directed energy deposition
Heterogenous structure
Strength-ductility synergy
Plastic deformation
316 L stainless steel

ABSTRACT

Achieving a favorable balance between strength and ductility remains a critical challenge in additive manufacturing (AM) of structural metals. This study proposes a universally applicable design strategy based on layer-wise in-situ alloying, which enables flexible and coordinated control over composition and architecture within a single-alloy system. Using 316 L stainless steel as a model material, titanium (Ti) was selectively introduced into alternating layers during laser-directed energy deposition (L-DED) to construct laminated structures comprising Ti-alloyed (hard) and pure (soft) domains. The resulting heterostructures exhibit superior combinations of strength and ductility as compared to the homogenous samples. The high strength arises from the rule of mixture and hetero-deformation-induced (HDI) strengthening, while HDI strain hardening and twinning-induced plasticity (TWIP) delay necking and contribute to sustained ductility. Systematic investigations revealed that Ti content and laminate spacing critically influence microstructural heterogeneity and mechanical incompatibility due to the dilution phenomenon. Optimal mechanical performance was achieved with 1.5 wt.% Ti and a bilayer alloying pattern, yield a tensile strength of 726.1 MPa and uniform elongation of 41 %. These findings establish layer-wise in-situ alloying as a general design route for tailoring mesoscale heterogeneity and unlocking new performance regimes in AM-fabricated structural components.

1. Introduction

The pursuit of materials that simultaneously exhibit high strength and ductility remains a central challenge in materials science and engineering [1,2]. Structural alloys, particularly those used in demanding applications such as aerospace, nuclear, and biomedical industries, must balance these properties to ensure both safety and performance. Most conventional strengthening strategies, such as cold working [3], ceramic particle reinforcement [4], or solid solution alloying [5], often improve strength at the expense of ductility, adhering to the classic strength-ductility trade-off. This compromise stems from the inherent competition between dislocation accumulation (which enhances strength) and dislocation mobility (which governs ductility). Consequently, overcoming this trade-off requires innovative approaches to microstructural design.

Recent advances in heterogeneous structure design offer a promising pathway to transcend this dilemma [6,7]. Unlike homogeneous materials, heterogeneous materials exploit mechanical incompatibilities between distinct microstructural domains (e.g., soft/hard phases, coarse/fine grains, or gradient compositions) to generate strain gradients at hetero-interfaces. These gradients promote the accumulation of geometrically necessary dislocations (GNDs) and resultant hetero-deformation-induced (HDI) stresses, which simultaneously enhance strength through HDI strengthening and delay necking via sustained strain hardening [8]. Among various heterogenous architectures, laminated structures, composed of alternating soft and hard layers, have garnered particular interest. Their high interfacial density amplifies HDI effects, while the periodic arrangement of soft/hard layers

* Corresponding authors.
E-mail addresses: gxzhu@suda.edu.cn (G. Zhu), lijq@suda.edu.cn (J. Li), xingzhang@suda.edu.cn (X. Zhang).
[1] Y. Wang and Q. Hu contribute equally as co-first authors
[2] Present address: 8 Jixue Road, Suzhou, Jiangsu, 215000, China (Xing Zhang)

https://doi.org/10.1016/j.jmatprotec.2025.118998
Received 17 April 2025; Received in revised form 15 July 2025; Accepted 27 July 2025
Available online 28 July 2025

enables tunable stress redistribution and crack deflection. However, conventional fabrication methods, such as diffusion bonding [9], accumulative roll bonding [10], or powder metallurgy [11], face critical limitations. These processes often struggle to control layer thickness, minimize interfacial defects (e.g., delamination, porosity), or fabricate geometrically complex components, restricting their industrial scalability and applicability.

Additive manufacturing (AM), particularly directed energy deposition (DED) [12], offers a revolutionary alternative. The layer-by-layer deposition inherent to AM enables precise spatial control over composition and microstructure, making it uniquely suited for fabricating architectured materials with tailored heterogeneities. Recent studies have demonstrated the potential of DED to produce laminated structures combining different alloys. For example, Pan et al. [13] fabricated a laminated structure consisting of 316 L stainless steel (SS) and 18Ni 300 maraging steel by wire-arc DED, achieving a tensile strength of 850 MPa with 12 % elongation that exceeds the rule-of-mixtures predictions. Similarly, Xu et al. [14] employed laser DED (L-DED) to fabricate a 316 L/17–4PH laminated steel composites, and claimed that strain partitioning and transformation-induced plasticity contributed to improved strength and ductility. Nevertheless, these efforts largely rely on material paring, where micro-mechanical incompatibility arises from the intrinsic properties of two distinct alloys. This reliance restricts compositional flexibility, introduces potential interfacial mismatch or defects, and limits the ability to systematically optimize mechanical performance.

To move beyond these constraints, a fundamental question arises: how can compositional heterogeneity and architectural configuration be flexibly and coordinately controlled within a single-alloy system to achieve mechanical synergy? In particular, it remains unclear how spatial compositional variation, when deliberately integrated with architectural features, affects microstructure evolution, strain distribution and micro-mechanical incompatibility in additively manufactured heterostructures. The relationship between compositional design, structural configuration, and deformation behavior remains insufficiently understood.

In this study, we leverage the in-situ alloying strategy, a widely used approach in AM for tailoring local composition, and extend it toward a new mode of control. Specifically, we implement a layer-wise, selective doping method, in which alloying elements are introduced only into designated layers during L-DED. This enables systematic modulation of compositional and architectural parameters, offering a powerful means to engineer heterogeneous structures within a single-alloy system. Using 316 L SS as a representative base material, we introduce titanium (Ti) into alternating layers to construct a laminated architecture comprising Ti-alloyed (hard) and pure (soft) domains. This model system allows us to investigate how Ti content and laminate spacing affect microstructure evolution, strain partitioning, and mechanical incompatibility. Through combined microstructural characterization and mechanical testing, we uncover how the interplay between composition and architecture governs deformation behavior, and demonstrate a tunable pathway for achieving strength-ductility synergy. Our findings demonstrate a broadly applicable strategy for designing hetero-structured metallic materials and provide new insights into the mesoscale control of heterogeneity in AM-fabricated structures.

2. Materials and methods

2.1. Materials and L-DED process

Spherical powders of 316 L SS and TA1 pure Ti (Avimetal) with diameter ranged in 53–105 μm were employed as raw materials for this study, as shown in Fig. 1a and 1b. To prepare the feedstock, 316 L SS powders were mixed with Ti additions of 1 wt.%, 1.5 wt.% and 2 wt.% using a planetary ball mill operated at a rotation speed of 200 rpm, ball-to-powder ratio of 4:1, and milling time of 6 h. Rectangular plates of cast 316 L SS with a dimension of 100 mm × 100 mm × 10 mm were used as the substrate for L-DED experiments. Thin-walled cubic specimens measuring 70 mm × 30 mm × 3 mm were deposited using a DED system with annular laser beam under the following conditions: laser power of 1000 W, scanning speed of 4 mm/s, spot diameter of 2.5 mm, powder feeding rate of 8.6 g/min and layer thickness of 0.7 mm. Two structural configurations were prepared for comparisons: homogeneous (M) and layered heterogeneous structures (H). The homogeneous samples were fabricated entirely from a single powder source, while the hetero-structured sample were achieved by alternately delivering 316 L

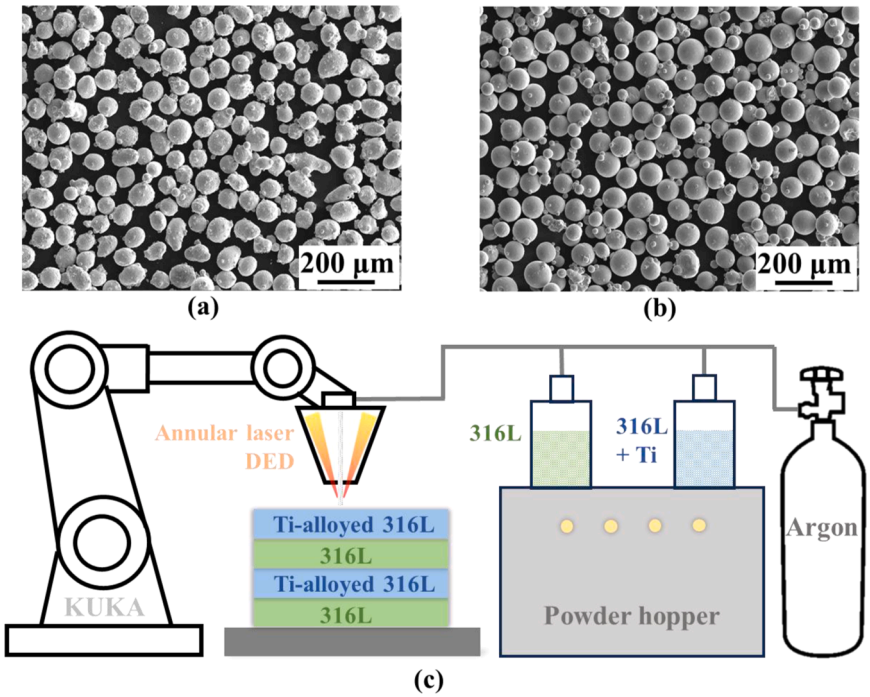

Fig. 1. Powders and experimental process: (a-b) Powder morphologies of 316 L SS (a) and Ti (b); (c) schematics of L-DED process for hetero-structured 316 L SS.

powder and 316 L+Ti powder mixture to the L-DED system, as shown in Fig. 1c.

2.2. Microstructure analysis

Prior to microstructure characterization, the as-built samples were cross-sectioned, followed by grinding and polishing. Subsequently, the polished surfaces were etched with aqua regia (hydrochloric acid: nitric acid = 3:1) for 25 s. The macrostructure of heterogenous samples were examined by optical microscope (OM, VHX-E20). The microstructure and fractography were observed using scanning electron microscope (SEM, TESCAN VEGA3) operated at 10 kV. The elemental distributions were characterized by energy-dispersive X-ray spectroscopy (EDS) at an accelerating voltage of 15 kV. In addition, nano-scale microstructure was characterized using a transmission electron microscope (TEM, FEI Tecnai F30). Moreover, samples polished by vibratory polisher were examined by electron backscatter diffraction (EBSD, ZEISS GeminiSEM 300) to obtain the crystalline grain structure and phase composition. EBSD data were acquired using accelerating voltage of 20 kV, with variable step sizes (2 μm for larger regions and 0.4 μm for finer-scale details).

2.3. Mechanical testing

Microhardness measurements were conducted using a Vickers hardness tester (Mega Instruments) with a load of 300 g and a dwell time of 15 s. Miniature tensile specimens were machined via electrical discharge machining (EDM) with a gauge length of 10 mm, width of 2.5 mm, and thickness of 1.2 mm. Uniaxial tensile tests were performed at room temperature using a mechanical testing machine (KPL Focal 100U2) at a strain rate of 0.001 s^{-1}. In-situ strain mapping during tensile deformation was performed using digital image correlation (DIC, LINCONST LVE 5 M) to track local strain evolution during deformation.

3. Results

3.1. Microstructure of homogenous Ti-alloyed 316 L SS

The microstructural evolution of Ti-alloyed 316 L SS was systematically investigated to understand the effects of Ti addition on grain morphology, phase composition, and elemental segregation. EBSD analyses of homogeneous samples reveal significant variations in grain structure with increasing Ti content (M0, M1, M2, M3, corresponding to 0 wt.%, 1 wt.%, 1.5 wt.%, and 2 wt.% Ti, respectively). According to the inverse pole figure (IPF) map shown in Fig. 2a, the M0 sample without Ti addition exhibited a microstructure dominated by large columnar grains (average size: 31.68 μm) aligned along the build direction, a characteristic feature of AM process due to steep thermal gradients and epitaxial growth during layer-by-layer deposition. Notably, finer equiaxed grains were observed at interlayer regions, likely resulting from partial remelting and rapid solidification between successive deposition passes [15].

With incremental Ti additions, a progressive transition from columnar to equiaxed grain morphology was observed (Fig. 2b-d). The M1 sample (1 wt.% Ti) displayed a bimodal structure comprising both columnar and equiaxed grains, with the average grain size reduced to 16.27 μm. Further refinement occurred in M2 (1.5 wt.% Ti) and M3 (2 wt.% Ti), where equiaxed grains dominated, achieving average sizes of 15.38 μm and 13.90 μm, respectively (Fig. 2m-p). This grain refinement aligns with Ti's role as a potent grain growth inhibitor. During solidification, Ti segregates to grain boundaries, increasing constitutional undercooling and restricting grain coarseness by impeding boundary migration [16]. Concurrently, the maximum intensity observed in the {001} pole figures (Fig. 2i-l) decreased from 3.78 in M0 to 1.45 in M3, indicating a progressive weakening of crystallographic texture [17,18]. This trend suggests that Ti disrupts the directional solidification pathways, promoting heterogeneous nucleation.

Phase composition analysis (Fig. 2e-h) revealed that Ti addition significantly altered the phase distribution. The M0 sample consisted predominantly of austenite (FCC phase, ~99.1 %) with trace ferrite (BCC phase, ~0.9 %). With Ti additions, the BCC phase fraction increased progressively to 1.3 % (M1), 4.4 % (M2), and 5.6 % (M3). This phase evolution is attributed to Ti's strong ferrite-stabilizing effect, which shifts the solidification sequence from austenite-dominated (A mode) to ferrite-austenite (FA) or fully ferritic (F mode) regimes. Notably, in M3, localized regions exhibited island-like BCC phases embedded within the FCC matrix, indicative of incomplete diffusion during rapid cooling.

To further understand the microstructural changes induced by Ti, sub-grain morphology was examined using SEM and EBSD, as shown in Fig. 3. The M0 sample exhibited a classic cellular structure, a common feature of rapidly solidified austenitic stainless steels processed by AM. With the addition of 1 wt.% Ti, noticeable microstructural modifications were observed. Specifically, lath-like features began to appear within the grains, indicating the onset of sub-grain boundary rearrangement. Further Ti additions led to the progressive disappearance of the cellular morphology and the emergence of a denser lath structure. In the M3 sample, the lath boundaries became less continuous, and a large number of fine particles were observed along sub-grain boundaries. EBSD characterization further confirmed that these lath structures were aligned with both sub-grain and high-angle grain boundaries. Their formation is likely associated with localized elemental segregation during solidification. Notably, a secondary morphology consisting of isolated island-like FCC phases also emerged in Ti-alloyed samples, particularly in M2 and M3, which was absent in the Ti-free sample.

To examine the elemental segregation, TEM coupled with EDS analysis was performed. The results, shown in Fig. 4a and b, revealed pronounced segregation of Mo and Ti at the sub-grain/grain boundaries. This observation is consistent with prior findings in AM-processed 316 L, where ferrite-stabilizing elements such as Mo and Cr are rejected into inter-cell regions during primary austenite solidification [19]. The continuous enrichment of these elements at inter-dendritic boundaries facilitates the formation of minor amounts of BCC ferrite phase. The EDS mapping also indicated significant Ti enrichment along sub-grain boundaries, often co-located with Mo/Cr-rich regions. These areas likely correspond to Ti- and Mo-containing intermetallic precipitates. The selected area electron diffraction (SAED) pattern and corresponding point EDS (Fig. 4c) scan suggest that these precipitates are Ti-enriched FeMoCr χ (chi) phase with a BCC crystal structure [20,21]. Obviously, the segregation of Ti plays a critical role in microstructure evolution. Firstly, as a strong ferrite stabilizer, Ti segregation enhances the formation of the BCC phase at sub-grain/grain boundaries. Secondly, it likely alters the solidification mode from the conventional A mode toward FA or F modes. This explains the appearance of island-like ferrite regions embedded within the FCC matrix. Additionally, the presence of Ti increases the growth restriction factor, enhancing constitutional undercooling ahead of the solid-liquid interface and thereby promoting grain refinement.

3.2. Microstructure of laminated heterogeneous 316 L SS/Ti-alloyed 316 L SS

To investigate the formation and evolution of heterogeneous laminated structures, a series of samples were fabricated by alternately depositing one layer of pure 316L and one layer of Ti-alloyed 316 L using L-DED. Three configurations (H1-S, H2-S, and H3-S) were designed, corresponding to Ti additions of 1 wt.%, 1.5 wt.%, and 2 wt.% in the Ti-alloyed layers, respectively. This design enabled a controlled evaluation of how increasing the compositional contrast between adjacent layers affects the resulting microstructural heterogeneity.

As shown in Fig. 5, OM observations along the building direction revealed well-defined layer-wise features, characterized by alternating

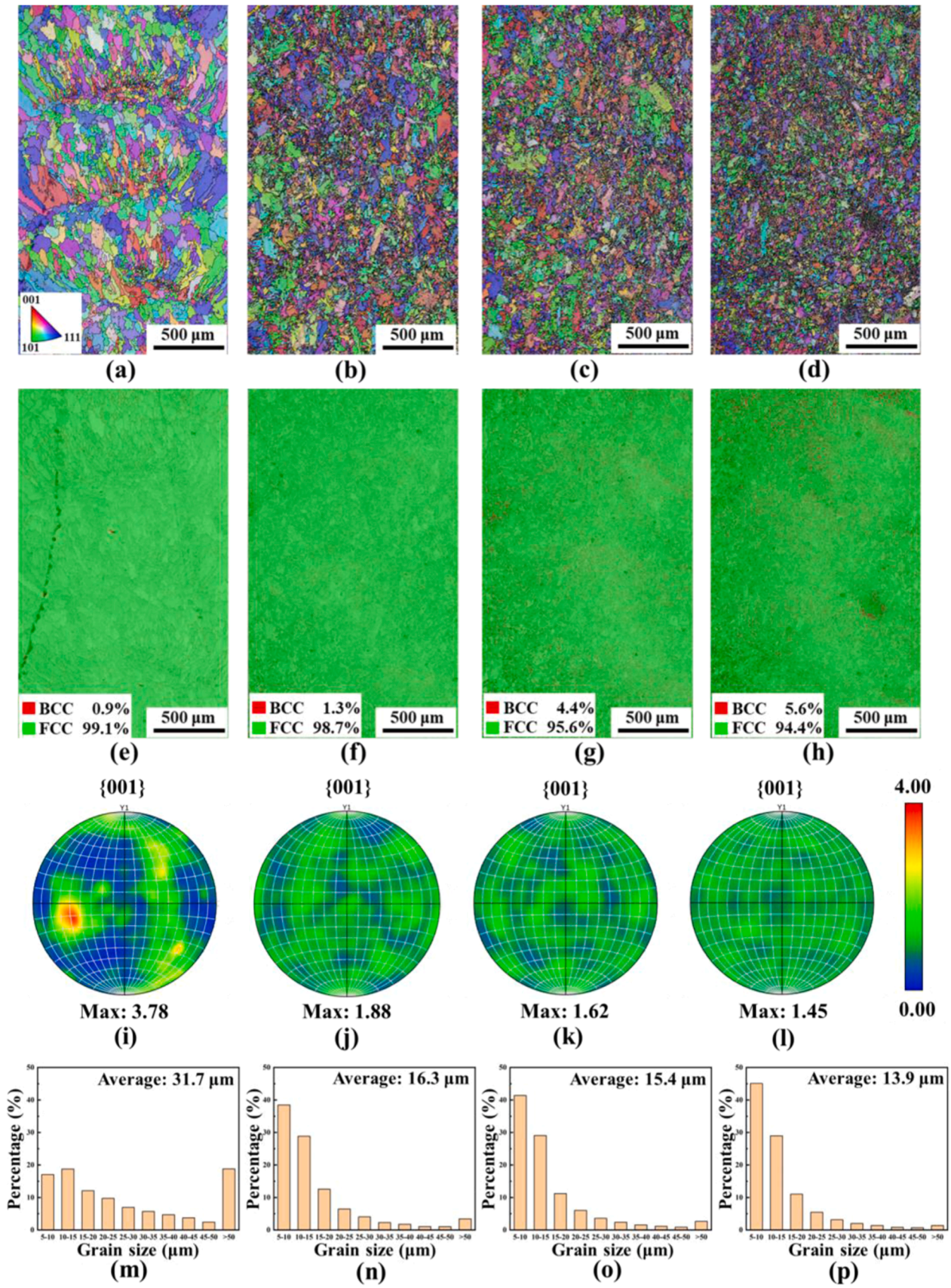

Fig. 2. Microstructure of as-built homogenous Ti-alloyed 316 L SS: (a-d) IPF maps showing the grain morphology; (e-h) Phase maps showing the volume fraction of FCC and BCC phases; (i-l) Pole figures corresponding to the dominant FCC phase; (m-p) Grain size distributions. Each row, from left to right, represents M0 (0 wt.% Ti), M1 (1 wt.% Ti), M2 (1.5 wt.% Ti), and M3 (2 wt.% Ti) samples, respectively.

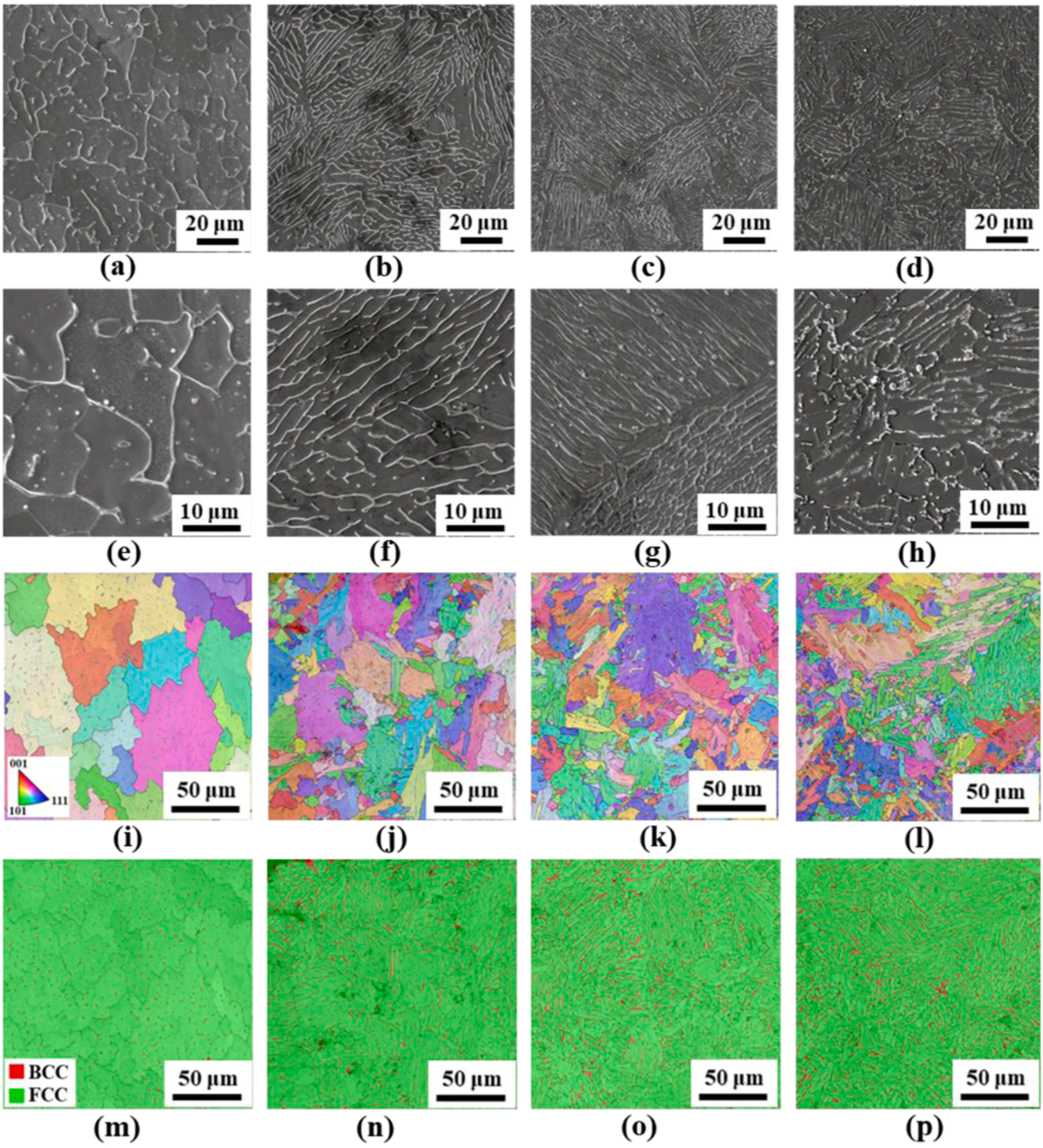

Fig. 3. Sub-grain microstructure of as-built homogenous Ti-alloyed 316 L SS: (a-d) high-magnification secondary electron (SE) images; (e-h) enlarged SE images; (i-l) high-magnification IPF maps; (m-p) phase maps showing the distribution of BCC phase. Each row, from left to right, represents M0, M1, M2, and M3 samples, respectively.

bright and dark regions. The bright bands corresponded to the pure 316 L layers, while the darker bands represented the Ti-alloyed 316 L layers, attributed to their relatively inferior corrosion resistance under the etching condition. The EBSD results confirmed clear differences in grain morphology and size between the two regions, particularly in the H1-S sample. In this configuration, the 316 L region retained a columnar grain structure with significant epitaxial growth, whereas the Ti-alloyed region exhibited finer, equiaxed grains. The interface between the coarse and fine-grained regions was clearly identified, reflecting a high degree of microstructural contrast.

As the Ti content was increased to 1.5 wt.% in the H2-S sample, the grain morphology within the 316 L region began to change. Although the Ti-alloyed layers still exhibited refined equiaxed grains, the adjacent 316 L layers displayed shorter and narrower columnar grains, indicating an influence from the Ti-alloyed layers during subsequent deposition. The distinct interface observed in H1-S became less apparent in H2-S,

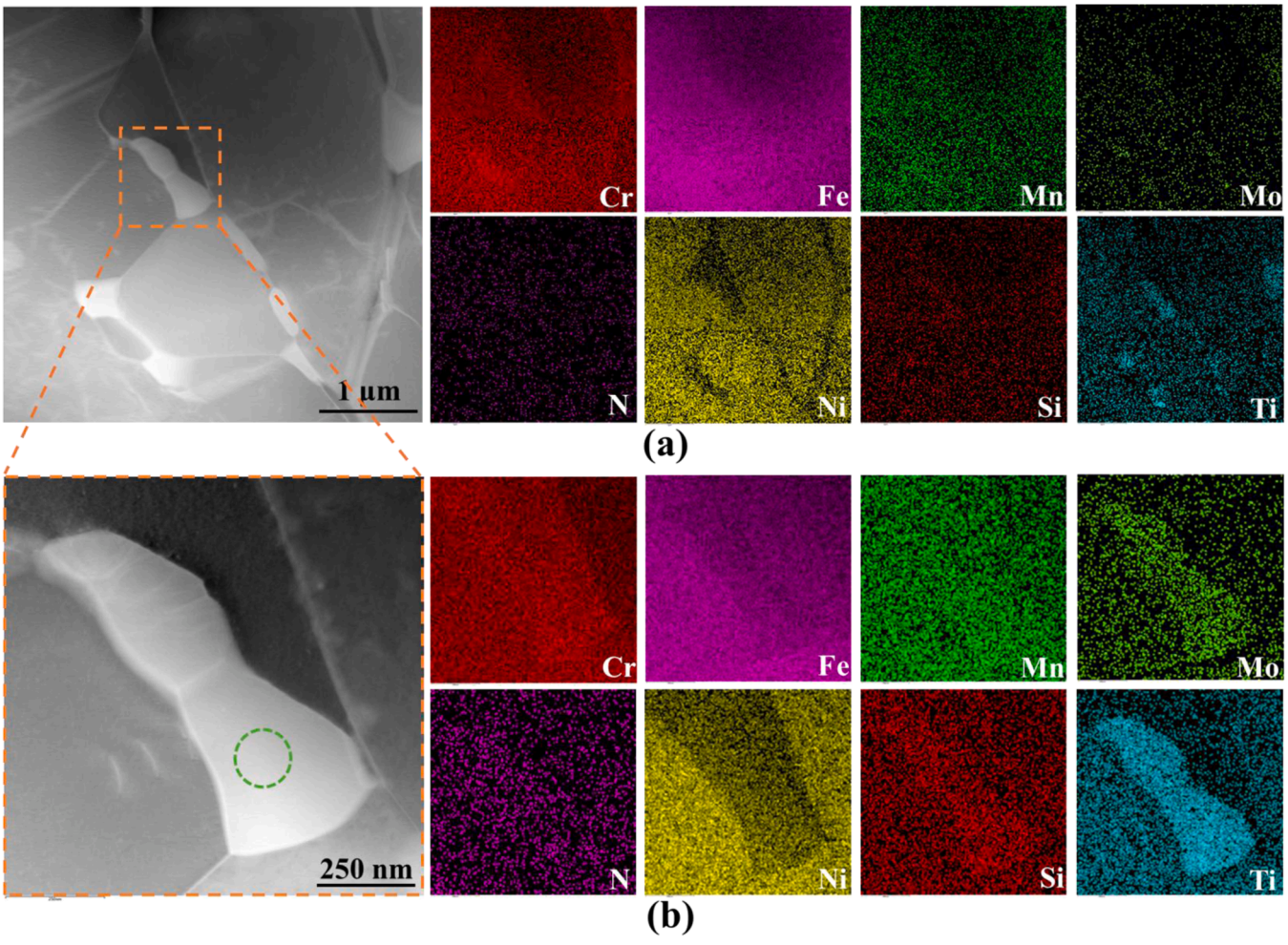

Elements	wt/.%
Fe	56.6
Cr	20.2
Mo	8.5
Ti	5.5
Ni	5.4
Other	3.8

(c)

Fig. 4. (a) TEM image of the M3 sample showing multiple precipitates at the grain boundary along with elemental mapping; (b) Magnified view of the boxed region in (a), revealing local elemental segregation around the precipitates; (c) Selected area electron diffraction (SAED) pattern and point EDS analysis obtained from the precipitate at the green dashed circle in (b).

suggesting partial grain structure homogenization across layers. With further increase in Ti content to 2 wt.% (H3-S sample), the grain structure across both the Ti-alloyed 316 L and pure 316 L layers became increasingly similar. The entire build exhibited predominantly fine equiaxed grains with minimal visible transition between layers. These observations indicate that with higher Ti addition, the microstructural heterogeneity originally present between layers becomes diminished.

The alteration of microstructural contrast is likely caused by dilution phenomenon that occurs during the L-DED process. The repeated laser passes required for each new layer result in partial remelting of the previously deposited material. When Ti-alloyed material is deposited atop pure 316 L, convective mixing within the melt pool under Marangoni flow facilitates interlayer diffusion of Ti. Consequently, the composition and microstructure of the upper region of the 316 L layer are modified, reducing the sharpness of the layer interface and weakening the heterogeneity.

To clarify the extent of elemental diffusion and its impact on microstructural evolution, further analyses of interlayer regions were performed using SEM and EDS mapping. In the H1-S sample, three representative regions were examined: the Ti-alloyed layer, the upper

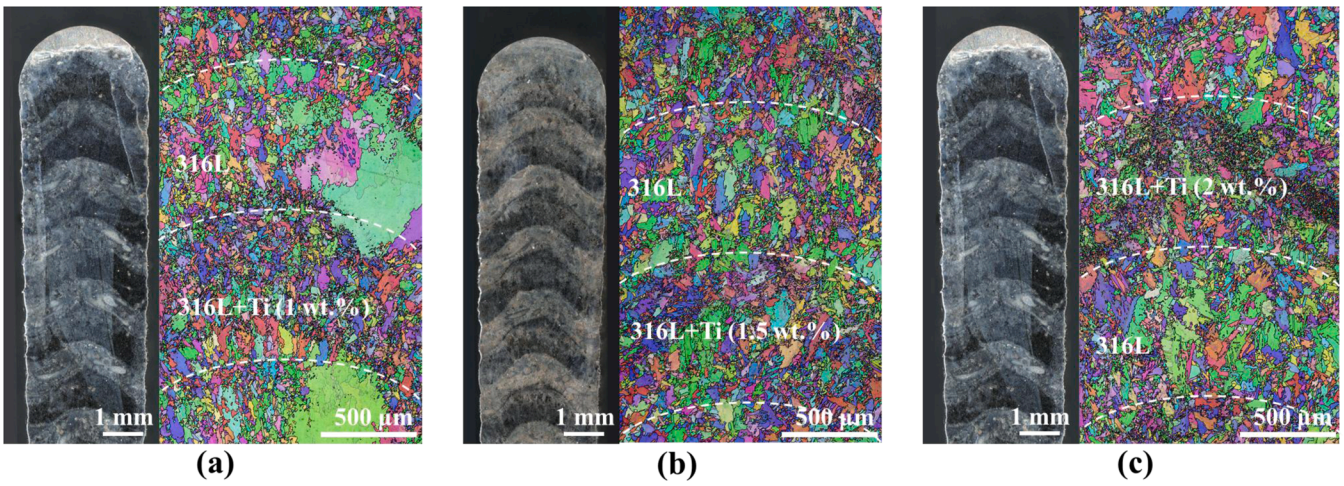

Fig. 5. OM images and EBSD IPF maps of laminated heterogeneous 316 L SS: (a) H1-S; (b) H-2S; (c) H3-S.

region of adjacent 316 L layer, and the adjacent 316 L layer. As shown in Fig. 6, the Ti-alloyed region (red square) exhibited the expected lath-like structure with a Ti content of approximately 0.79 wt.%, slightly lower than the nominal composition due to diffusion. The adjacent 316 L region (blue square) retained a cellular structure typical of AMed 316 L and exhibited a minimal Ti content of 0.21 wt.%, indicating limited interdiffusion. In the upper portion of the 316 L layer (yellow square), which lies directly beneath the next Ti-alloyed layer, the Ti content slightly increased to 0.33 wt.% and the microstructure remained predominantly cellular structure. These results suggest that in the H1-S sample, the influence of Ti diffusion on the 316 L region was minimal and spatially confined near the interface.

A different behavior was observed in the H2-S sample, where the Ti content in the 316 L layers was notably higher. As shown in Fig. 7, the Ti-alloyed region maintained a dense lath-like structure with a measured Ti content of 1.36 wt.%, again slightly below the intended 1.5 wt.% due to dilution. The upper region of the adjacent 316 L layer showed a microstructure transitioning from cellular to lath-like, accompanied by increased Ti content reaching up to 0.48 wt.%. Even the middle region of the 316 L layer contained approximately 0.33 wt.% Ti and exhibited partial morphological modification. These results indicate a more significant interdiffusion of Ti compared to H1-S, resulting in a dilution effect that extended deeper into the pure 316 L layer.

In the H3-S sample, where the Ti content reached 2 wt.%, the dilution phenomenon became even more pronounced. As illustrated in Fig. 8, the Ti-alloyed layer exhibited dense lath-like features with a Ti content close to 1.8 wt.%. Remarkably, the 316 L layers also exhibited similar lath-like structures, with EDS measurements revealing Ti contents as high as 0.75 wt.% and 1.25 wt.% in the middle and upper portions, respectively. Cellular features were nearly absent, and the

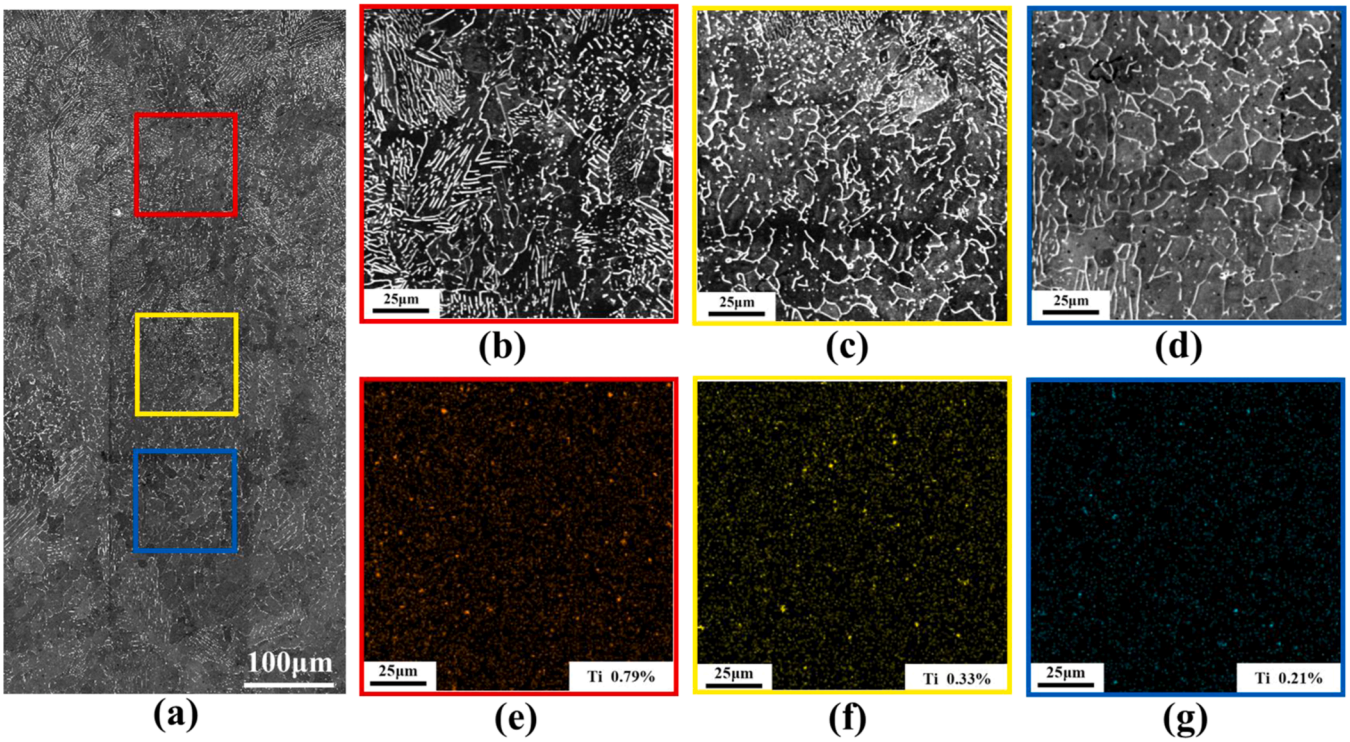

Fig. 6. SE imaging and EDS analysis of H1-S (1 wt.% Ti): (a) Low magnification image showing microstructure variation across different regions; (b-d) High magnification images of Ti-alloyed layer (b), upper region of 316 L layer (c), 316 L layer (d); (e-g) Ti distribution in corresponding regions.

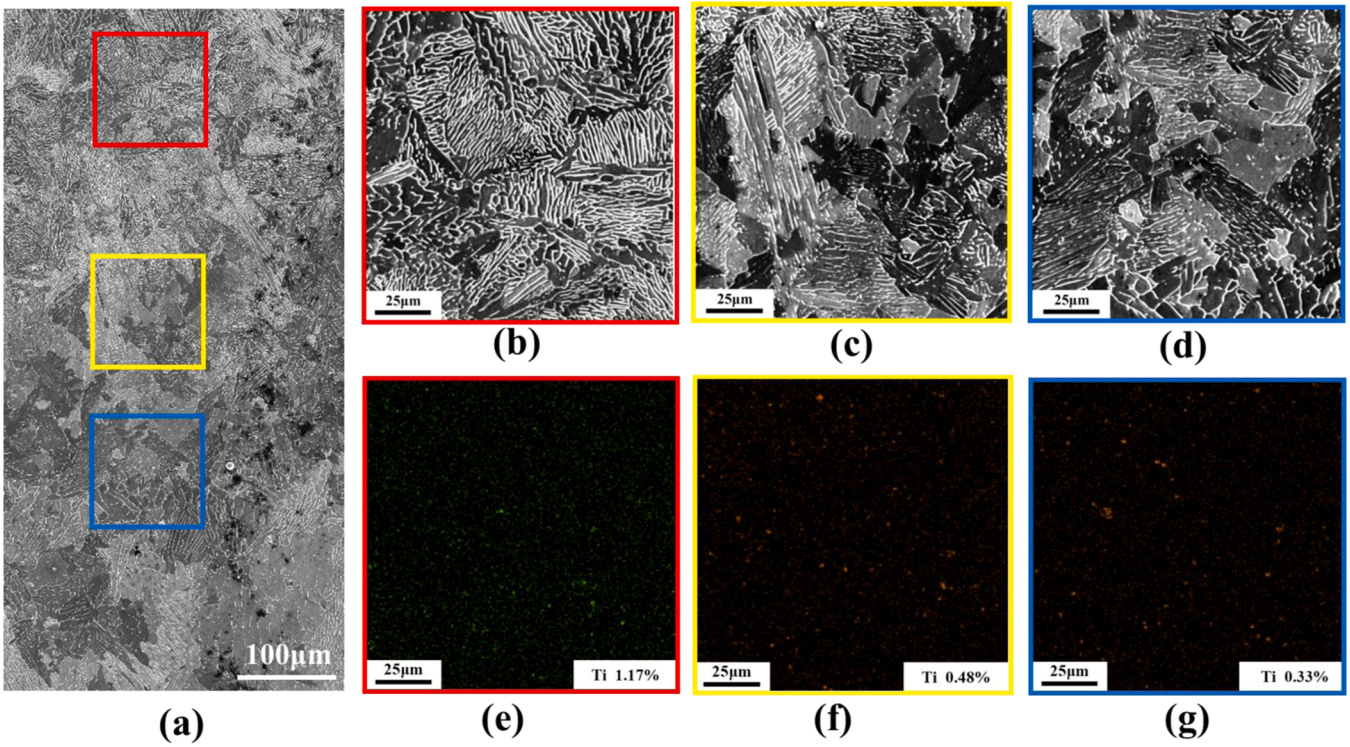

Fig. 7. SE imaging and EDS analysis of H2-S (1.5 wt.% Ti): (a) Low magnification image showing microstructure variation across different regions; (b-d) High magnification images of Ti-alloyed layer (b), upper region of 316 L layer (c), 316 L layer (d); (e-g) Ti distribution in corresponding regions.

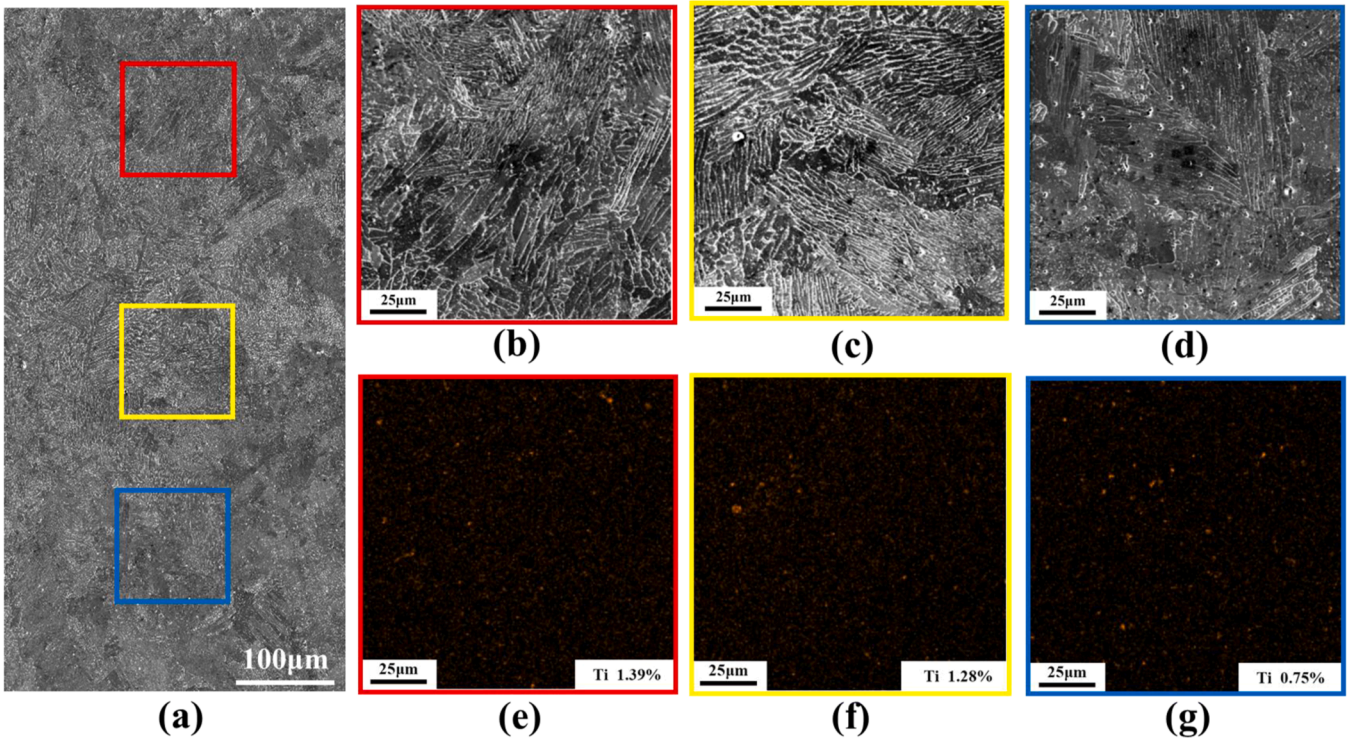

Fig. 8. SE imaging and EDS analysis of H3-S (2 wt.% Ti): (a) Low magnification image showing microstructure variation across different regions; (b-d) High magnification images of Ti-alloyed layer (b), upper region of 316 L layer (c), 316 L layer (d); (e-g) Ti distribution in corresponding regions.

original layered architecture was visually indistinct in terms of grain morphology. These findings suggest that at high Ti concentrations, substantial interlayer mixing occurs, which effectively eliminates the microstructural contrast initially designed into the system.

The above characterization results demonstrate that the microstructure of the laminated heterogeneous 316 L/Ti-alloyed 316 L samples is highly sensitive to Ti content due to melt pool dynamics during L-DED processing. At lower Ti contents (1 wt.%), the structural

heterogeneity is well preserved, with clearly defined layer interfaces and contrasting grain morphologies. As Ti content increases, enhanced Marangoni convection and solute diffusion promote elemental mixing, leading to partial homogenization of the microstructure across layers. This gradual loss of heterogeneity directly impacts the strain partitioning behavior and HDI effect, as discussed in subsequent sections.

To counteract excessive homogenization observed at higher Ti contents, two additional sample sets were fabricated using modified deposition strategies. In these configurations, the Ti-alloyed layers (1.5 wt% Ti) were deposited every two (H2-D) or three layers (H2-T), rather than alternately with each pure 316 L layer. As shown in Fig. 9, OM imaging revealed more widely spaced Ti-alloyed bands with preserved layer boundaries. The EBSD results confirmed the re-emergence of clear grain structure differences between layers. In contrast to H2-S, the pure 316 L regions in H2-D and H2-T maintained large columnar grains, while the Ti-alloyed regions retained fine equiaxed grains. Although some diffusion into adjacent 316 L layers was still present, the overall microstructural heterogeneity was effectively restored. This demonstrates that by adjusting laminate spacing, it is possible to mitigate interdiffusion and preserve designed structural contrasts.

3.3. *Microhardness and tensile properties of laminated hetero-structured 316 L SS*

The mechanical properties of both homogeneous and laminated heterogeneous samples were evaluated through microhardness measurements and uniaxial tensile testing, with particular emphasis on understanding how Ti content and laminate architecture influence strength and ductility. Vickers microhardness measurements revealed a direct correlation between Ti content and hardness in homogeneous samples (Fig. 10a). The pure 316 L SS (M0) exhibited an average hardness of 201 HV, consistent with conventional AMed 316 L. With incremental Ti additions, hardness increased linearly to 216 HV (M1, 1 wt.% Ti), 238 HV (M2, 1.5 wt.% Ti), and 245 HV (M3, 2 wt.% Ti). This trend in hardness reflects the cumulative effects of multiple strengthening mechanisms including grain refinement, solid solution strengthening, and dislocation strengthening, as discussed in Subsection 4.1.

In hetero-structured samples, microhardness profiles exhibited periodic fluctuations corresponding to alternating soft (pure 316 L) and hard (Ti-alloyed 316 L) layers. As shown in Fig. 10b-d, the hardness contrast between adjacent layers became more pronounced with increasing Ti content. To be specific, in the H1-S sample (1 wt.% Ti), the soft zone exhibited average hardness values of ~204 HV, while the hard zone reached ~218 HV. This difference became more significant in the H2-S sample (1.5 wt.% Ti), where the soft region measured approximately 207 HV and the hard region increased to ~238 HV. These results highlight the effectiveness of the in-situ alloying strategy in engineering controlled mechanical heterogeneity at the mesoscale. More importantly, the ability to precisely tune this hardness contrast by adjusting Ti content provides a versatile approach to designing strain-partitioning architectures that promote HDI strengthening, as discussed in Section 4.2. It is also noteworthy that at 2 wt.% Ti (H3-S), the hardness of the soft region further increased to ~210 HV due to the dilution effect, while the hard region slightly increased to ~242 HV. This suggests that the interlayer hardness difference approaches a saturation point beyond which further Ti addition yields may reduce micro-mechanical contrast. Additionally, the H2-D and H2-T samples (Fig. 10e and f), also exhibited pronounced alternating hardness profiles between soft and hard layers (similar to H2-S), confirming the effectiveness and reproducibility of the heterostructure architecture.

Uniaxial tensile tests highlighted significant differences between homogeneous and hetero-structured samples. For homogeneous samples, a typical strength-ductility trade-off was observed with increasing Ti addition, as shown in Fig. 11a. The ultimate tensile strength (UTS) increased significantly from 598.8 MPa in M0 to 671.1 MPa (M1), 741.5 MPa (M2), and 792.8 MPa (M3). However, this increase in strength came at the cost of ductility, as the total elongation decreased from 56.0 % in M0 to 39.29 %, 30.90 %, and 27.70 % in M1, M2, and M3, respectively. This trend is consistent with the conventional understanding that strengthening mechanisms such as grain refinement and solid solution hardening reduce strain hardening capability and accelerate strain localization, leading to early fracture.

In contrast, the laminated heterogeneous samples exhibited a markedly improved balance between strength and ductility (Fig. 11b and c). All hetero-structured configurations achieved tensile properties that surpassed the strength-ductility envelope established by the homogeneous samples. The H1-S sample exhibited a UTS of 658.0 MPa and total elongation of 49.0 %, while H2-S reached 681.3 MPa with 46.6 % elongation, and H3-S achieved 705.9 MPa with 41.3 % elongation. Although the strength of these samples increased with Ti content, the reduction in ductility was much less severe compared to their homogeneous counterparts. The influence of laminate architecture was further examined in the H2-D and H2-T samples, in which the Ti-alloyed (1.5 wt.%) layers were deposited every two or three layers, respectively, instead of alternating layer-by-layer. This design modification aimed to mitigate excessive Ti diffusion while preserving mechanical heterogeneity. Tensile testing revealed a pronounced dependence of strength-ductility synergy on laminate spacing. The H2-D sample exhibited remarkable enhanced performance, with a UTS of 726.1 MPa and total elongation of 48.2 %, a 4.9 % increase in UTS and 3.4 % improvement in ductility compared to the alternating-layer H2-S configuration. In contrast, the H2-T sample displayed reduced efficacy, with UTS and

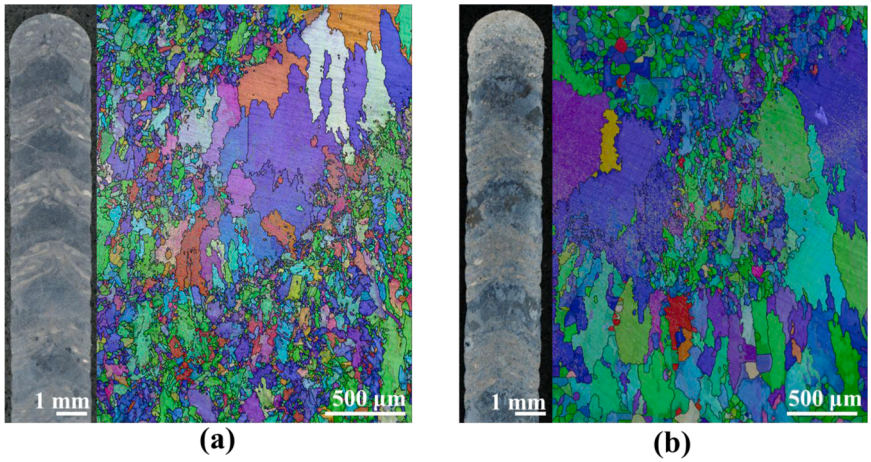

Fig. 9. OM images and EBSD IPF maps of (a) H2-D and (b) H-2T samples.

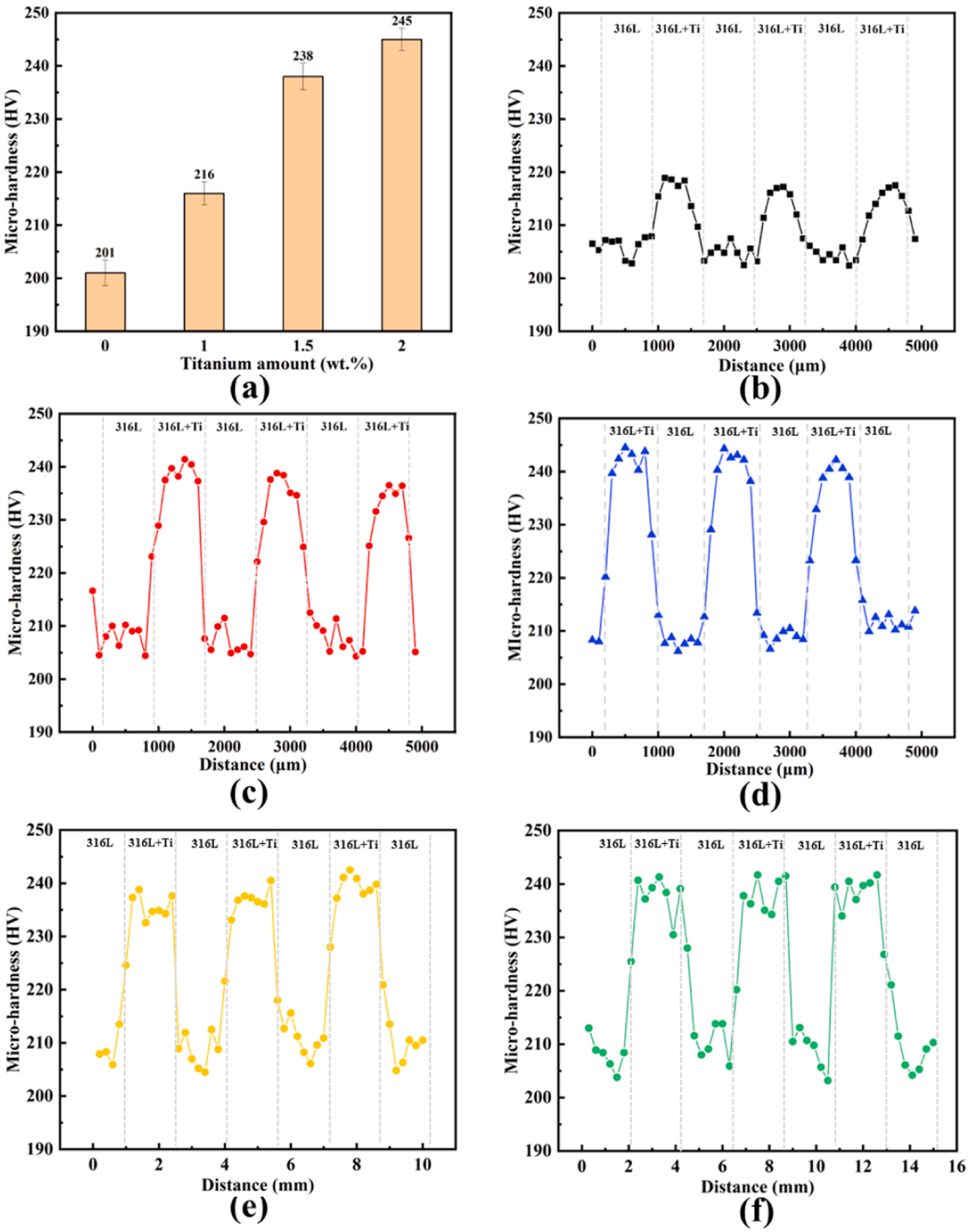

Fig. 10. Microhardness profiles: (a) Average microhardness of homogeneous Ti-alloyed 316 L; (b-f) Periodic fluctuations in hetero-structured samples H1-S (b), H2-S (c), H3-S (d), H2-D (e), H2-T (f), reflecting soft/hard layer contrasts.

total elongation declining to 685.9 MPa and 42.9 %, respectively. These results demonstrate that that both mechanical contrast and laminate spacing play critical roles in tailoring mechanical response of hetero-structured 316 L SS.

To provide a broader perspective, Fig. 11d compares the optimized tensile properties of the present work with previous literature reports on AM-fabricated 316 L, alloyed 316 L, 316L-based composites and bimetallic heterogenous structures as well as conventionally manufactured 316 L (details in Table S1). It is evident that the hetero-structured samples in this study outperform most previously reported counterparts in terms of UTS-uniform elongation combinations, showing outstanding strain hardening capability. This highlights the effectiveness of the layer-wise in-situ alloying strategy not only in enhancing individual mechanical properties but also in overcoming the conventional trade-off between strength and ductility.

Fractographic analysis further supports the mechanical test results. As shown in Fig. 12a–d, the fracture surface of the M0 sample was dominated by uniform and high-density dimples, indicative of a ductile

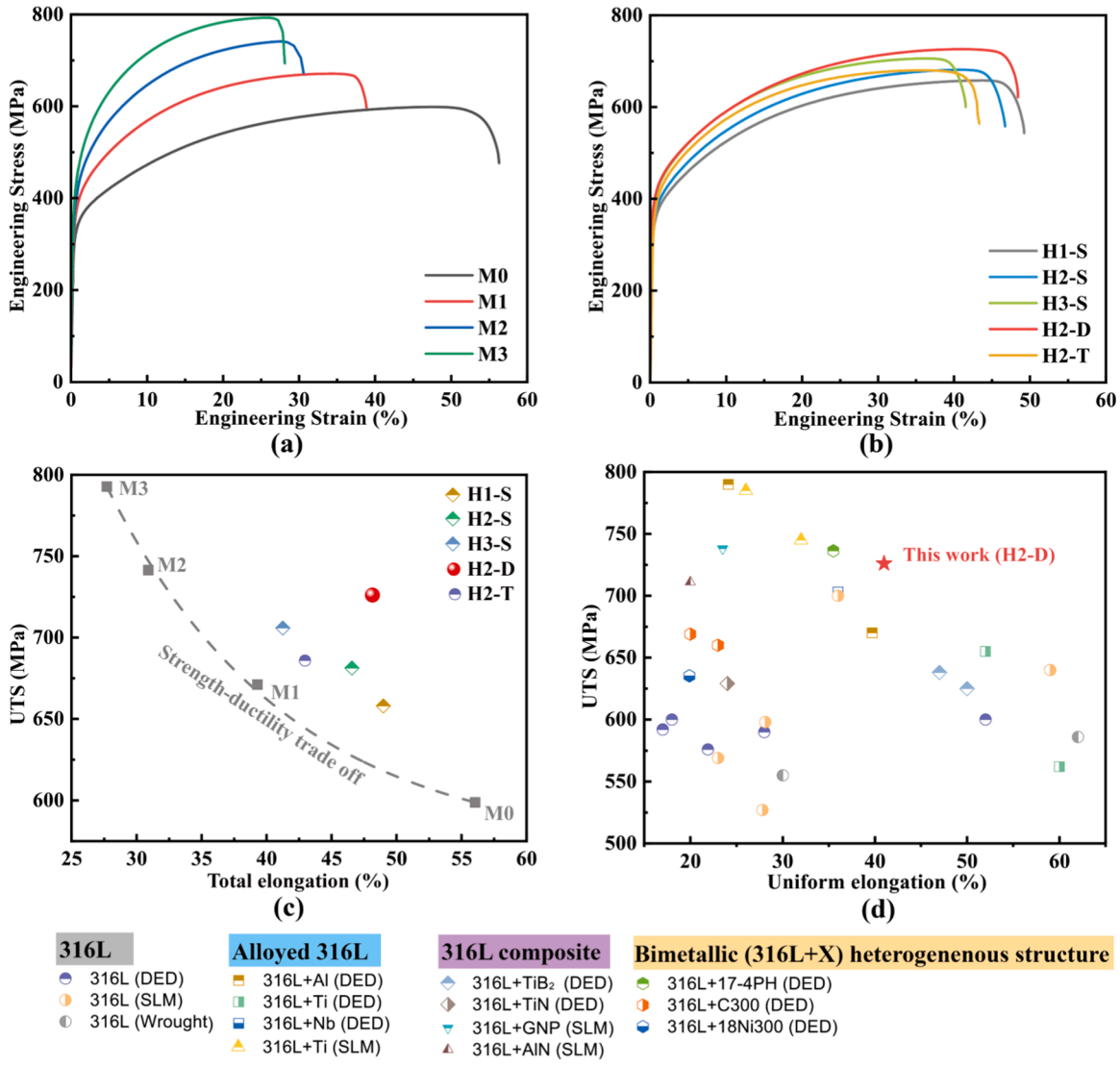

Fig. 11. Uniaxial tensile properties: (a) Representative tensile engineering stress-strain curves of homogeneous Ti-alloyed 316 L SS; (b) Representative tensile engineering stress-strain curves of laminated heterogeneous 316 L SS; (c) Strength-ductility comparison among homogenous and heterogeneous samples; (d) UTS versus uniform elongation of the optimal H2-D sample as compared with 316 L SS related materials fabricated by conventional and AM approaches.

fracture mode. With increasing Ti addition, the dimple size increased while their density decreased, suggesting a transition toward more localized deformation. In the M3 sample, quasi-cleavage features (highlighted by yellow arrows) were observed, suggesting the presence of brittle fracture components, likely associated with intermetallic phase formation at high Ti content. In the hetero-structured samples, fracture consistently occurred within the soft 316 L regions. Fig. 12e–i reveals mixed morphologies of micro- and submicron-sized dimples in laminated configurations, notably in H2-S and H2-D samples (highlighted by yellow circles), evidencing enhanced strain accommodation and delayed crack propagation. These fractographic features corroborate the superior strength-ductility synergy observed in tensile testing and support the role of HDI-induced strain hardening in sustaining ductility under elevated stress conditions.

4. Discussion

4.1. Strengthening mechanism by Ti addition in AMed 316 L SS

To systematically evaluate the strengthening mechanisms of Ti-alloyed 316 L SS fabricated via AM, quantitative analysis of yield strength contributions was performed. One of the main strengthening mechanisms is grain refinement strengthening ($\Delta\sigma_{gr}$), which occurs as grain boundaries act as barriers to dislocation motion, as described by the Hall-Petch relationship:

$$\Delta\sigma_{gr} = k_{HP}\left(\frac{1}{\sqrt{d_r}} - \frac{1}{\sqrt{d_0}}\right) \quad (1)$$

where k_{HP} is the Hall-Petch coefficient (267 MPa·μm$^{1/2}$ for 316 L SS [22]), d_o represents the average grain size of 316 L SS (31.7 μm based on the EBSD results), d_r is refined grain size with Ti addition, which decreases to 16.3, 15.4, and 13.9 μm for M1, M2, M3 samples, respectively. The estimated contributions of grain refinement ($\Delta\sigma_{gr}$) to yield strength are calculated to be 18.7, 20.6, and 24.2 MPa for 1 wt.%, 1.5 wt.%, and 2 wt.% Ti addition, respectively.

Solid solution strengthening is an important phenomenon for austenite steel, which arises due to lattice distortion caused by solute atoms, impeding dislocation motion. According to the study by Zwagg et al. [23], the solid solution strengthening contribution ($\Delta\sigma_{ss}$) can be expressed as:

$$\Delta\sigma_{ss} = (k_i c_i)^n \quad (2)$$

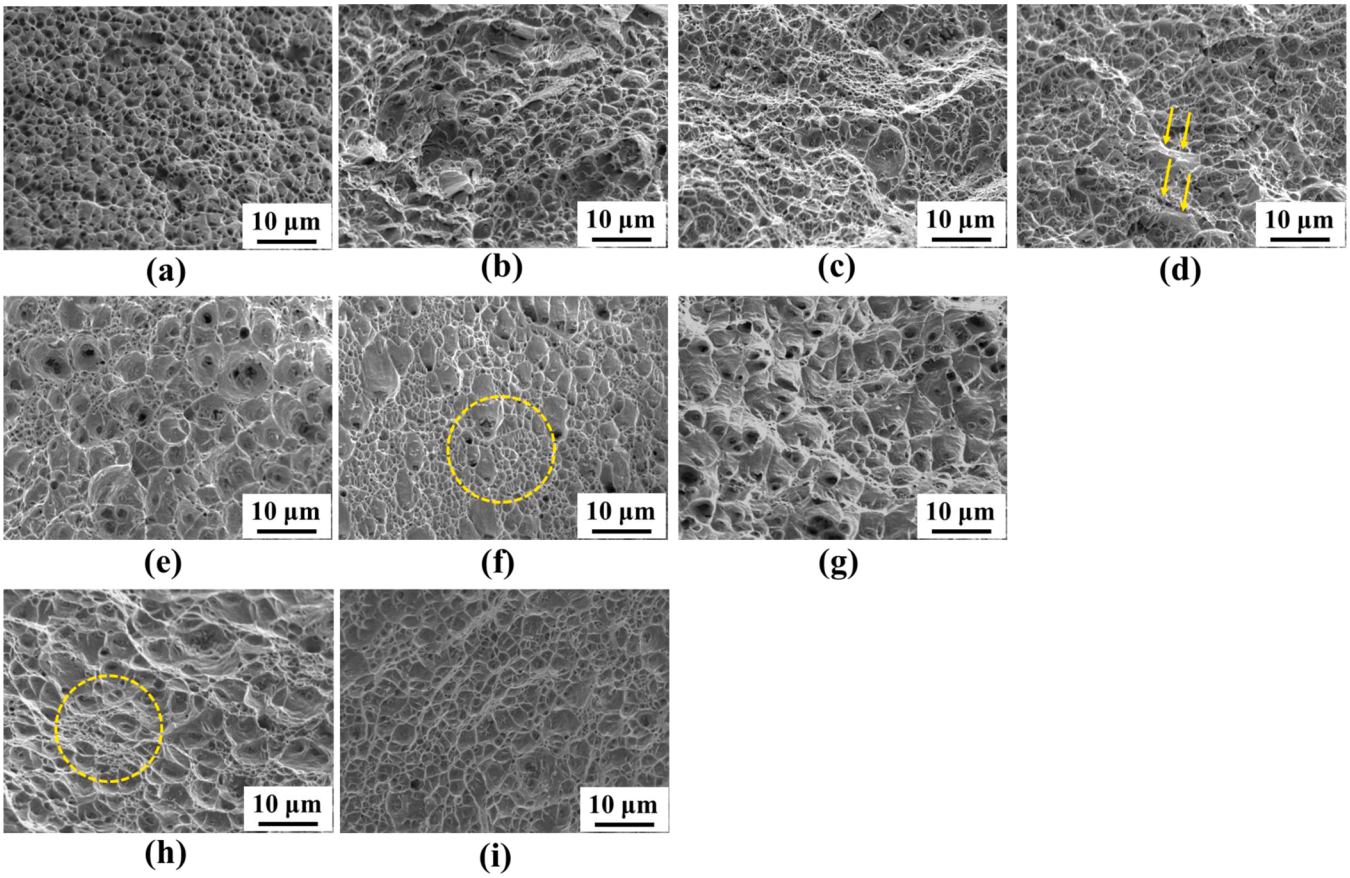

Fig. 12. Fracture morphologies: (a-d) fracture morphologies of homogeneous M0, M1, M2, M3, respectively; (e-g) fracture morphologies of hetero-structured H1-S, H2-S, H3-S, respectively; (h, i) fracture morphologies of hetero-structured H2-D and H2-T, respectively.

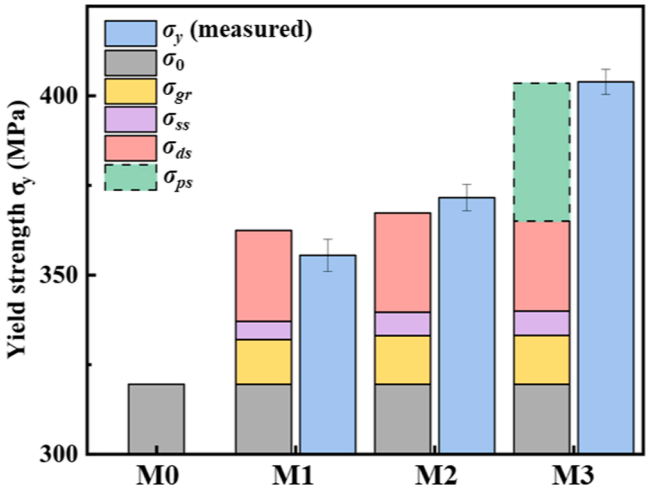

Fig. 13. Calculated and measured yield strengths of M0, M1, M2, M3 samples.

where k_i is the strengthening coefficient for 1 at% of alloying element (17.9 MPa/at% for Ti in stainless steel), c_i is atomic fraction of alloying element, and n is generally taken as 2/3 for FCC systems. The calculated values of solid solution strengthening contribution are 7.6 MPa, 9.9 MPa, 12.0 MPa for 1 wt%, 1.5 wt%, and 2 wt% Ti addition, respectively.

Moreover, dislocation strengthening plays a crucial role due to the rapid solidification inherent in AM processes, which generates high dislocation densities to accommodate residual plastic strain [2]. The strengthening contribution from dislocations ($\Delta\sigma_{ds}$) can be estimated using the Taylor equation [24]:

$$\Delta\sigma_{ds} = M\alpha bG\left(\sqrt{\rho_r} - \sqrt{\rho_0}\right) \tag{3}$$

where M is the Taylor factor (3.06), α is a coefficient related to dislocation type (0.2), b is the Burgers vector (0.256 nm), G is the shear modulus (78 GPa), ρ_0 and ρ_r are the dislocation density of 316 L and Ti-alloyed 316 L, respectively. While the total dislocation population is comprised of both geometrically necessary dislocations (GNDs) and statistically stored dislocations, previous investigations [25] have indicated that GND constitutes the majority of total dislocations in AMed FCC metals. Using measured GND values from EBSD data (1.8×10^{13}, 5.4×10^{13}, 5.9×10^{13}, 6.2×10^{13} m^{-2} for M0, M1, M2, M3, respectively), the dislocation strengthening contributions are estimated to be 37.9 MPa, 42.0 MPa and 44.4 MPa for 1 wt.%, 1.5 wt.%, and 2 wt.% Ti addition, respectively.

The cumulative effect of these strengthening mechanisms on the yield strength can be estimated using the root sum square relationship [26]:

$$\sigma_y = \sigma_0 + \sqrt{\Delta\sigma_{gr}{}^2 + \Delta\sigma_{ss}{}^2 + \Delta\sigma_{ds}{}^2} \tag{4}$$

where σ_0 is the yield strength of additively manufactured M0 sample without Ti addition (319.5 MPa). As shown in Fig. 10, the calculated yield strengths for M1 and M2 samples (362 and 367 MPa, respectively) show good agreement with experimental results (355.5 MPa and 371.6 MPa, respectively), confirming the reliability of the predictions. However, for M3 (2 wt.% Ti), the experimentally measured yield strength (403.9 MPa) significantly exceeds the predicted value

(371.4 MPa), suggesting the presence of an additional strengthening mechanism. Based on the microstructure analysis in Fig. 4, Ti-enriched intermetallic particles were formed at the grain and sub-grain boundaries in the M3 sample, which could further enhance material strength by Orowan strengthening ($\Delta\sigma_{ps}$). Thus, the predicted yield strength can be modified as:

$$\sigma_y = \sigma_0 + \sqrt{\Delta\sigma_{gr}{}^2 + \Delta\sigma_{ss}{}^2 + \Delta\sigma_{ds}{}^2 + \Delta\sigma_{ps}{}^2} \quad (5)$$

The strengthening contribution from dispersion particles $\Delta\sigma_{ps}$ can be calculated by the Orowan equation [26]. Due to the non-uniform size and distribution of Ti-enriched particles, direct calculation of Orowan strengthening is challenging; however, backward calculation using experimental data gives an estimated value of 66.3 MPa for M3 sample.

Consequently, the findings indicate that dislocation strengthening is the dominant mechanism in AMed 316 L SS with small amounts of Ti addition, contributing more significantly to strength enhancement than grain refinement and solid solution strengthening. However, at higher Ti levels (2 wt.%), intermetallic phase formation introduces an additional Orowan strengthening effect, further elevating the yield strength. It is important to note that while these strengthening mechanisms effectively enhance material strength, they also contribute to the classic strength-ductility trade-off, posing challenges in optimizing Ti content to achieve the desired mechanical performance.

4.2. *Mechanism responsible for the enhanced strength-ductility synergy of hetero-structured 316 L SS*

To elucidate the impact of structural heterogeneity on deformation behavior, in-situ two-dimensional DIC measurements were conducted to capture the local strain distribution during tensile testing, as shown in Fig. 14. The strain distribution along the tensile axis reveals that, at low strain levels, both M0 and H2-S samples exhibit relatively uniform strain distribution along the gauge length. However, with increasing strain, distinct deformation patterns emerge. In the M0 sample (pure 316 L SS), significant strain localization can be observed, exhibiting a characteristic 45° inclination that is consistent with the direction of maximum shear stress (indicated by the white dashed square in Fig. 14a). This

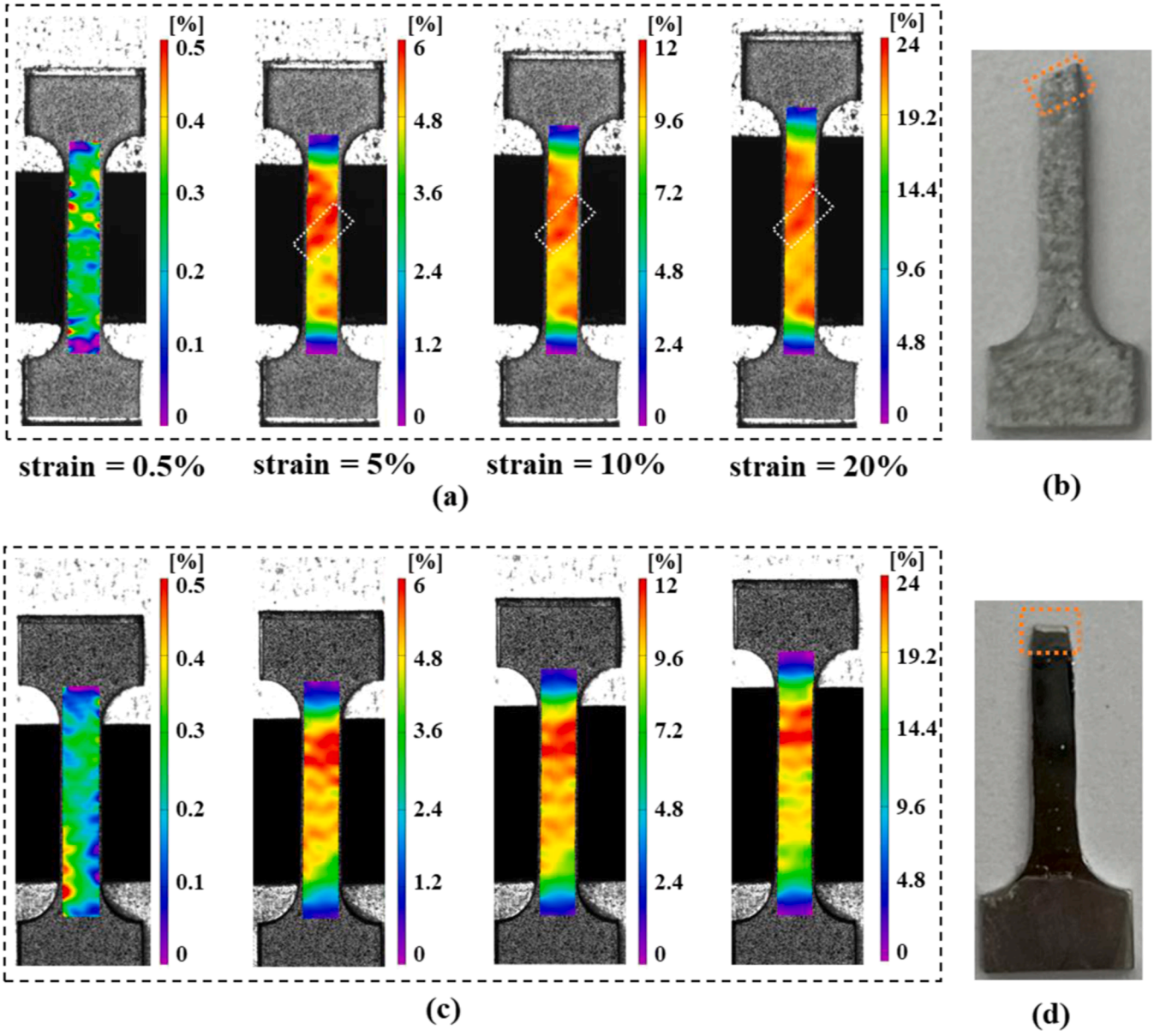

Fig. 14. Strain distribution upon monotonic tensile tests: (a, c) In-situ DIC strain maps during tensile tests of M0 (a) and H2-S (c) samples; (b, d) Fracture direction of M0 (b) and H2-S (d) samples.

localized zone expands with further straining, culminating in necking and an inclined fracture morphology (Fig. 14b). In contrast, the H2-S sample, featuring alternating 316 L and Ti-alloyed 316 L domains, displays a distinct strain distribution pattern beyond the early deformation stage. Due to the mechanical contrast between the softer 316 L and harder Ti-alloyed 316 L domains, plastic deformation preferentially occurs in the 316 L layers, resulting in strain partitioning (Fig. 14c). This behavior persists at higher strains, generating local strain differences of 3 % - 5 % across adjacent domains and establishing a significant strain gradient across the microstructure. Additionally, the H2-S sample develops multiple discrete strain localization regions, which is beneficial to delay necking and promote a transverse fracture morphology (Fig. 14d).

Microstructural analysis was conducted to further investigate the effects of strain partitioning on deformation behavior. High-resolution back-scatter electron (BSE) imaging reveals prominent deformation

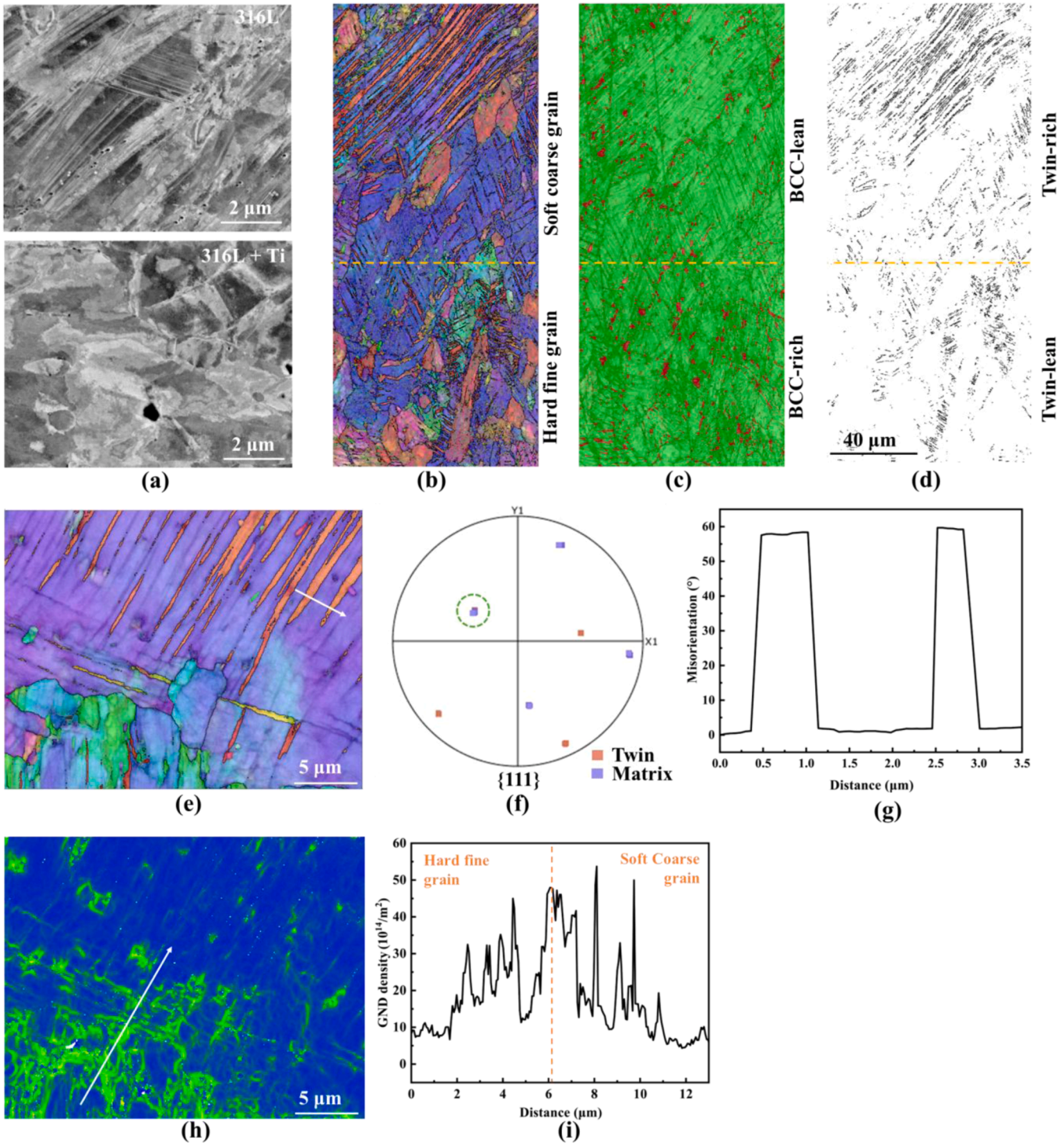

Fig. 15. Microstructural characterization of tensile-fractured heterogenous sample: (a) BSE images of 316 L and Ti-alloyed 316 L domains; (b-d) Low magnification EBSD analysis near interface region between fine grain and coarse grain domains: IPF map (b), phase map (c) and special boundary (Σ3) map (d). High-magnification EBSD analysis near region of coarse-fine grain domains: (e) IPF map;(f) {111} pole figure; (g) the misorientation profile along the white arrow in (e); (h) GND map; (i) The GND profile along the white arrow in (h).

bands within the 316 L domain, whereas such features are notably absent in the Ti-alloyed 316 L domain (Fig. 15a). EBSD analysis further highlights this deformation incompatibility (Fig. 15b-d). Specifically, in the softer coarse-grained regions with minimal BCC phase, extensive deformation bands are observed. High-magnification IPF maps (Fig. 15e) identify these bands as deformation twins (width less than 1 μm), confirmed by a ~60° misorientation from the point-to-origin profile (Fig. 15g), typical characteristic of {111}< 112 > deformation twins (Σ3) [27]. To further confirm the twinning nature of these bands, the pole figure analysis was conducted. As shown in Fig. 15f, the matrix and twin domains share a common {111} pole (highlighted by a green dashed circle), consistent with the mirror symmetry characteristic of Σ3 twins. In contrast, the finer-grained Ti-enriched regions, which contain a higher fraction of the BCC phase, exhibit significantly reduced twinning due to grain refinement and lattice distortion by Ti addition. In these regions, dislocation slip becomes the dominant deformation mechanism. Notably, it is evident that GNDs formed within the softer 316 L domain to accommodate strain gradients were effectively blocked at the interfaces with the harder Ti-alloyed 316 L domain, leading to dislocation pile-ups at the soft-hard interfaces (Fig. 15h and i). Such dislocation accumulation generates long-range back stress in the softer domain, impeding dislocation motion and thereby enhancing material strength. This HDI strengthening, combined with the conventional rule of mixture ($\sigma=\Sigma V_i\sigma_i$, where V_i and σ_i are the volume fraction and strength of individual constitute material, respectively [28]), contributed to the overall enhanced strength of heterostructure material.

Simultaneously, the HDI effect accelerates dislocation accumulation, enhancing strain hardening capacity. This enables the material to maintain uniform deformation under elevated stress, mitigating premature localization and improving ductility [29]. In addition, the elevated back stresses may have acted as a driving force to activate secondary deformation mechanisms such as twinning, further amplifying the twinning-induced plasticity (TWIP) effect in the 316 L regions. Similar findings have been reported in the literature, such as in the study by Shi et al. [30], which demonstrated that hetero-structured eutectic high-entropy alloys exhibited twinning activation near soft/-hard interfaces to alleviate local stress concentrations induced by GND pile-up. Consequently, these synergistic mechanisms from HDI strengthening and strain hardening as well as enhanced TWIP contributes to the superior strength-ductility balance observed in the hetero-structured 316 L/Ti-alloyed 316 L system. These findings reinforce the concept that deliberate microstructural heterogeneity can be harnessed to modulate and enhance deformation behavior in AM-fabricated alloys.

4.3. *Effect of heterostructure configuration on the mechanical properties*

Mechanical incompatibility between constituent domains is a critical determinant of hetero-deformation behavior. Prior studies have [31] demonstrated that greater mechanical incompatibility (i.e., hardness differentials between adjacent domains) leads to higher strain gradients. In such cases, the soft-hard interface effectively blocks GND migration, requiring a higher back-stress level before yielding occurs in the hard regions, thereby enhancing HDI strengthening effects. In this study, increasing Ti content led to a pronounced hardness differential between 316 L and Ti-alloyed 316 L layers (demonstrated in Fig. 10), which significantly improved the HDI effect (Fig. 16a). This accounts for the strength increase from 658 MPa in H1-S to 681.3 MPa in H2-S, with only a marginal ductility reduction from 49.0 % to 46.6 % (Fig. 11a). This demonstrates that a moderate increase in mechanical contrast can improve strength without significantly compromising ductility. However, excessive Ti addition (e.g., 2 wt%) introduces complexities. Higher Ti levels exacerbate dilution effects, enlarging the dilution zone and reducing the Ti concentration differential between 316 L and Ti-alloyed

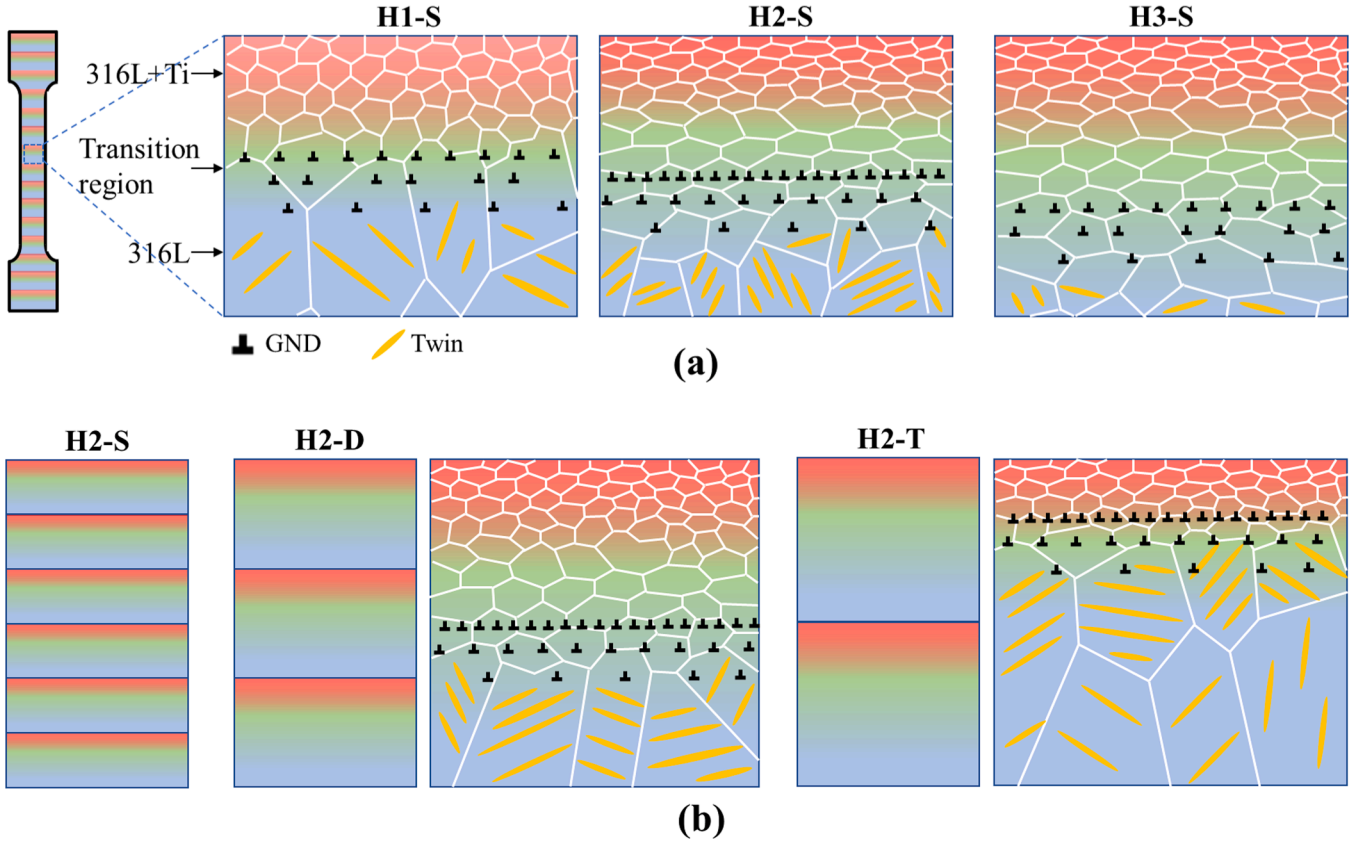

Fig. 16. Schematic illustration of deformation behavior for different heterostructure configuration: (a) Hetero-structured 316 L SS with different Ti additions and (b) with different laminate spacings.

316 L layers (e.g., Ti content difference decreases from 0.84 wt.% to 0.64 wt.% as Ti increases from 1.5 % to 2.0 %, according to Figs. 7 and 8). Consequently, this leads to the homogenization of grain structure, saturating or even reducing the mechanical incompatibility and the associated HDI effect. Additionally, excessive Ti addition promotes intermetallic phase formation at grain and sub-grain boundaries (Fig. 4), which embrittles the microstructure and degrades ductility. Moreover, the expanded dilution zone could reduce the volume fraction of coarse-grained 316 L regions, which are critical for sustaining high-stress twinning activity. This reduction in twinning capability also limits the strain-hardening capacity. Consequently, a substantial ductility loss was observed in hetero-structured 316 L SS at 2 wt.% Ti (total elongation of 41.3 %). These observations underscore the need for an optimal Ti content to balance HDI and TWIP contributions in layer-wise in-situ alloying strategies, a critical consideration for AM applications.

The necessity of balancing compositional contrast against diffusion-driven homogenization motivates the optimization of laminate architecture. While samples with 1.5 wt.% Ti exhibited favorable HDI strengthening, their grain structures lost distinct contrast (i.e., between columnar and equiaxed grains), reducing the designed mechanical disparity between the domains and twinning capability in 316 L layers. Increasing laminate spacing (e.g., alloying Ti every 2–3 layers) limits Ti infiltration into the 316 L layers, preserving undiluted 316 L regions and restoring a heterogeneous microstructure with alternating equiaxed and columnar grains (Fig. 16b). This configuration reinstates significant mechanical incompatibility, enhancing the HDI effect. Moreover, the expanded non-diluted 316 L regions, characterized by low stacking fault energy, provide ample space for twin formation under back stress, improving ductility at high strains. However, excessively thick laminates reduce the number of 316 L/Ti-alloyed 316 L domain interfaces, limiting GND pile-up sites and attenuating global HDI strengthening. Additionally, back stresses may not penetrate deeply enough into thicker 316 L domain to trigger widespread twinning, diminishing TWIP-mediated plasticity. Thus, an intermediate laminate thickness is essential to maximize the interplay between HDI and TWIP effects, offering a pathway to optimize strength-ductility synergy in hetero-structured alloys fabricated via AM.

Overall speaking, the mechanical performance of hetero-structured 316 L/Ti-alloyed 316 L is governed by a delicate interplay between composition, microstructure, and architecture. By precisely tuning Ti content and laminate spacing, it is possible to modulate mechanical heterogeneity, optimize HDI and TWIP effects, and achieve exceptional strength-ductility synergy. These insights offer valuable guidelines for the rational design of high-performance architectured metals via AM, with potential applications in aerospace, and marine components requiring tailored mechanical behavior.

5. Conclusions

In this study, we developed a layer-wise in-situ alloying strategy to fabricate tunable laminated heterostructures within single-alloy systems. Using 316 L SS as a model material, Ti was selectively doped into alternating layers via L-DED, enabling flexible control over compositional and architectural heterogeneities. The following key conclusions are drawn:

(1) Ti addition in AMed 316 L SS led to significant grain refinement, increased BCC phase fraction, and formation of sub-grain lath structures, enhancing strength through grain refinement, solid solution, dislocation, and Orowan mechanisms. However, excessive Ti (>1.5 wt.%) introduced intermetallic phases, exacerbating the strength-ductility trade-off.
(2) In hetero-structured samples, microstructural heterogeneity diminished with higher Ti content due to dilution effects. At 1 wt.% Ti, distinct columnar (316 L) and equiaxed (Ti-alloyed 316 L) grains formed, but increased Ti homogenized the grain structure. Moreover, increasing the Ti content could increase the micro-mechanical contrast, which was saturated upon 1.5 wt.%.
(3) Hetero-structured samples exhibited superior strength-ductility synergy compared to homogeneous counterparts, which was attributed to the HDI and TWIP effects. Below 1.5 wt.%, increasing Ti enhanced HDI effects due to larger micro-mechanical contrast, whereas excess Ti induced brittleness and suppressed TWIP, degrading ductility.
(4) Adjusting laminate spacing (e.g., alloying every two layers) preserved microstructural contrast by mitigating Ti dilution. Wider spacing maintained undiluted 316 L domains for sustained TWIP, while excessive spacing reduced interfacial HDI effects, highlighting the need for balanced architectural design.

This work provides fundamental insight into how microstructure evolution, strain partitioning, and micro-mechanical incompatibility can be systematically modulated through mesoscale chemical design. The findings establish clear links between compositional variations, architectural parameters, and deformation mechanisms, which are broadly relevant for the design of high-performance hetero-structured materials. Beyond the specific 316 L system, the demonstrated layer-wise alloying approach is applicable to a wide range of AM-compatible alloys and processing strategies where property tuning via localized heterogeneity is desirable. The methodology offers a scalable and generalizable route for tailoring microstructure-mechanics relationships in architectured parts. Future work may extend this strategy to lightweight alloys, functional gradients, or multi-principal element systems, potentially enabling site-specific performance optimization in structural or multifunctional components. This work thus provides not only a pathway for overcoming strength-ductility trade-offs, but also a design framework with relevance for both academic exploration and industrial adoption in advanced manufacturing.

CRediT authorship contribution statement

Yicheng Wang: Writing – original draft, Methodology, Investigation, Formal analysis. **Zhihong Yao:** Methodology, Investigation, Data curation. **Qihang Hu:** Writing – original draft, Methodology, Investigation, Formal analysis. **Gangxian Zhu:** Supervision, Resources, Funding acquisition. **Bo Mao:** Resources, Investigation, Data curation. **Xing Zhang:** Writing – review & editing, Supervision, Funding acquisition, Formal analysis, Conceptualization. **Jiaqiang Li:** Resources, Project administration, Investigation.

Declaration of Competing Interest

The authors declare that they have no known competing financial interests or personal relationships that could have appeared to influence the work reported in this paper.

Acknowledgements

This work was financially supported by the National Natural Science Foundation of China [grant numbers 52405399, 52475523]; the Sci-Tech Plan Project of Suzhou municipal of China [grant numbers SYC2022143].

Appendix A. Supporting information

Supplementary data associated with this article can be found in the online version at doi:10.1016/j.jmatprotec.2025.118998.

References

[1] Ritchie, R.O., 2011. The conflicts between strength and toughness. Nat. Mater. 10, 817–822. https://doi.org/10.1038/nmat3115.

[2] Wei, Y., Li, Y., Zhu, L., Liu, Y., Lei, X., Wang, G., Wu, Y., Mi, Z., Liu, J., Wang, H., Gao, H., 2014. Evading the strength-ductility trade-off dilemma in steel through gradient hierarchical nanotwins. Nat. Commun. 5, 3580. https://doi.org/10.1038/ncomms4580.

[3] Odnobokova, M., Belyakov, A., Kaibyshev, R., 2015. Effect of severe cold or warm deformation on microstructure evolution and tensile behavior of a 316L stainless steel. Adv. Eng. Mater. 17, 1812–1820. https://doi.org/10.1002/adem.201500100.

[4] Zhao, S., Shen, X., Yang, J., Teng, W., Wang, Y., 2018. Densification behavior and mechanical properties of nanocrystalline TiC reinforced 316L stainless steel composite parts fabricated by selective laser melting. Opt. Laser Technol. 103, 239–250. https://doi.org/10.1016/j.optlastec.2018.01.005.

[5] Chen, L., Wang, Y., Li, Y., Zhang, Z., Xue, Z., Ban, X., Hu, C., Li, H., Tian, J., Mu, W., 2025. Effect of nickel content and cooling rate on the microstructure of as cast 316 stainless steels. Crystals 15, 168. https://doi.org/10.3390/cryst15020168.

[6] Ma, E., Zhu, T., 2017. Towards strength–ductility synergy through the design of heterogeneous nanostructures in metals. Mater. Today 20, 323–331. https://doi.org/10.1016/j.mattod.2017.02.003.

[7] Chen, J., Han, Y., Wei, Z., Li, S., Sun, Z., Zhang, L., Huang, G., Le, J., Zhang, D., Lu, W., 2023. Heterostructured titanium composites with superior strength-ductility synergy via controllable bimodal grains and <c+a> dislocation activity. Mater. Res. Lett. 11, 863–871. https://doi.org/10.1080/21663831.2023.2252858.

[8] Zhu, Y., Wu, X., 2019. Perspective on hetero-deformation induced (HDI) hardening and back stress. Mater. Res. Lett. 7, 393–398. https://doi.org/10.1080/21663831.2019.1616331.

[9] Gao, D., Li, C., Zhang, C., Yang, B., Lin, T., Chen, L., Si, X., Qi, J., Cao, J., 2023. Microstructure and wettability of the micro-laminated Ti6Al4V/304 stainless steel composite fabricated by diffusion bonding. J. Mater. Res. Technol. 27, 3788–3796. https://doi.org/10.1016/j.jmrt.2023.10.219.

[10] Hosseini, M., Manesh, H.D., Eizadjou, M., 2017. Development of high-strength, good-conductivity Cu/Ti bulk nano-layered composites by a combined roll-bonding process. J. Alloy. Compd. 701, 127–130. https://doi.org/10.1016/j.jallcom.2017.01.048.

[11] Zhang, W., Yang, P., Cao, Y., Li, X., Wei, D., Kato, H., Wu, Z., 2021. New Ti/β-Ti alloy laminated composite processed by powder metallurgy: Microstructural evolution and mechanical property. Mater. Sci. Eng. A 822, 141702. https://doi.org/10.1016/j.msea.2021.141702.

[12] Svetlizky, D., Zheng, B., Vyatskikh, A., Das, M., Bose, S., Bandyopadhyay, A., Schoenung, J.M., Lavernia, E.J., Eliaz, N., 2022. Laser-based directed energy deposition (DED-LB) of advanced materials. Mater. Sci. Eng. A 840, 142967. https://doi.org/10.1016/j.msea.2022.142967.

[13] Pan, M., Xu, J., Liang, N., Peng, Y., Zhou, Q., Wang, K., 2023. Microstructure and mechanical properties of the laminated heterostructured material with 316L stainless steel/18Ni300 maraging steel fabricated by WAAM. Mater. Sci. Eng. A 881. https://doi.org/10.1016/j.msea.2023.145300.

[14] Xu, K., Li, B., Li, S., Chen, R., Gao, X., Liu, C., Jiang, C., Song, L., 2022. Excellent tension properties of stainless steel with a 316L/17-4PH/17-4PH laminated structure fabricated through laser additive manufacturing. Mater. Sci. Eng. A 833. https://doi.org/10.1016/j.msea.2021.142461.

[15] Liu, C.M., Tian, X.J., Tang, H.B., Wang, H.M., 2013. Microstructural characterization of laser melting deposited Ti–5Al-5Mo–5V–1Cr–1Fe near β titanium alloy. J. Alloy. Compd. 572, 17–24. https://doi.org/10.1016/j.jallcom.2013.03.243.

[16] Wang, S., Gao, Z., Wu, G., Mao, X., 2022. Titanium microalloying of steel: A review of its effects on processing, microstructure and mechanical properties. Int. J. Miner. Metall. Mater. 29, 645–661. https://doi.org/10.1007/s12613-021-2399-7.

[17] Todaro, C., Easton, M., Qiu, D., Zhang, D., Bermingham, M., Lui, E., Brandt, M., StJohn, D., Qian, M., 2020. Grain structure control during metal 3D printing by high-intensity ultrasound. Nat. Commun. 11, 1–9. https://doi.org/10.1038/s41467-019-13874-z.

[18] Zhang, G., Lu, X., Li, J., Chen, J., Lin, X., Wang, M., Tan, H., Huang, W., 2022. In-situ grain structure control in directed energy deposition of Ti6Al4V. Addit. Manuf. 55. https://doi.org/10.1016/j.addma.2022.102865.

[19] Wang, Y.M., Voisin, T., McKeown, J.T., Ye, J., Calta, N.P., Li, Z., Zeng, Z., Zhang, Y., Chen, W., Roehling, T.T., 2018. Additively manufactured hierarchical stainless steels with high strength and ductility. Nat. Mater. 17, 63–71. https://doi.org/10.1038/nmat5021.

[20] Zhang, S., Shi, X., Liang, Y., Xu, H., Yan, C., Yan, W., Rong, L., Yang, K., 2023. χ phase and its effect on the mechanical properties of a Mo-bearing high–Si austenitic stainless steel after aging at 650°. C. J. Mater. Res. Technol. 23, 4280–4292. https://doi.org/10.1016/j.jmrt.2023.02.069.

[21] Liu, H., Sun, He, Liu, B., Li, D., Sun, F., Zhang, Y., 2015. Analysis of χ phase precipitation in aged 2205 duplex stainless steel. J. Wuhan. Univ. Technol. Mater. Sci. Ed. 30, 591–595. https://doi.org/10.1007/s11595-015-1194-6.

[22] Zhai, W., Zhou, W., Nai, S.M.L., 2022. Grain refinement and strengthening of 316L stainless steel through addition of TiC nanoparticles and selective laser melting. Mater. Sci. Eng. A 832. https://doi.org/10.1016/j.msea.2021.142460.

[23] Lu, Q., Xu, W., van der Zwaag, S., 2014. Designing new corrosion resistant ferritic heat resistant steel based on optimal solid solution strengthening and minimisation of undesirable microstructural components. Comput. Mater. Sci. 84, 198–205. https://doi.org/10.1016/j.commatsci.2013.12.009.

[24] Lee, S.H., Chung, S.G., Kim, H.S., Cho, J.-W., 2023. Effects of AlN addition into AISI 316L on melt pool stability and microstructural evolution during laser powder bed fusion. Mater. Sci. Eng. A 881. https://doi.org/10.1016/j.msea.2023.145311.

[25] Smith, T.R., Sugar, J.D., San Marchi, C., Schoenung, J.M., 2019. Strengthening mechanisms in directed energy deposited austenitic stainless steel. Acta Mater. 164, 728–740. https://doi.org/10.1016/j.actamat.2018.11.021.

[26] AlMangour, B., Kim, Y.-K., Grzesiak, D., Lee, K.-A., 2019. Novel TiB2-reinforced 316L stainless steel nanocomposites with excellent room- and high-temperature yield strength developed by additive manufacturing. Compos. B Eng. 156, 51–63. https://doi.org/10.1016/j.compositesb.2018.07.050.

[27] Im, Y.-D., Kim, K.-H., Jung, K.-H., Lee, Y.-K., Song, K.-H., 2019. Anisotropic Mechanical Behavior of Additive Manufactured AISI 316L Steel. Metall. Mater. Trans. A 50, 2014–2021. https://doi.org/10.1007/s11661-019-05139-7.

[28] Tan, C., Chew, Y., Weng, F., Sui, S., Ng, F.L., Liu, T., Bi, G., 2022. Laser aided additive manufacturing of spatially heterostructured steels. Int. J. Mach. Tools Manuf. 172. https://doi.org/10.1016/j.ijmachtools.2021.103817.

[29] Zhu, Y., Wu, X., 2022. Heterostructured materials. Prog. Mater. Sci., 101019 https://doi.org/10.1016/j.pmatsci.2022.101019.

[30] Shi, P., Zhong, Y., Li, Y., Ren, W., Zheng, T., Shen, Z., Yang, B., Peng, J., Hu, P., Zhang, Y., 2020. Multistage work hardening assisted by multi-type twinning in ultrafine-grained heterostructural eutectic high-entropy alloys. Mater. Today 41, 62–71. https://doi.org/10.1016/j.mattod.2020.09.029.

[31] Wang, Y., Huang, C., Fang, X., Höppel, H., Göken, M., Zhu, Y., 2020. Hetero-deformation induced (HDI) hardening does not increase linearly with strain gradient. Scr. Mater. 174, 19–23. https://doi.org/10.1016/j.scriptamat.2019.08.022.